IJCESEN

ISSN : 2149-9144

International Journal of Computational and Experimental Science and ENgineering

ijcesen@gmail.com

dergipark.ulakbim.gov.tr/ijcesen

Founder-Editor-in-Chief : Prof.Dr. İskender AKKURT

Volume: 1 - No:2 - 2015

Preface

I am happy that *International Journal of Computational and Experimental Science and Engineering (IJCESEN)* published its second issue. There are 10 papers in this issue. All manuscripts were subjected to the peer review procedure. We appreciate all the authors and reviewers for their valuable contribution in order to achieve a publication of high scientific quality.

Prof.Dr. İskender AKKURT
Founder-Editor-in-Chief

Table of contents

International Journal of Computational and ExperimentalScience and Engineering (IJCESEN)
Vol. 1-No.2 (2015)pp. 1-6
http://dergipark.ulakbim.gov.tr/ijcesen

***ISSN:*2149-9144**

Modeling and simulation of 8-bit Current-Mode Successive Approximation Registers ADC by using Simulink

Toufik SMAIL[1]*, Salah HANFOUG[2] and Hocine BELMILI [1]

[1]U.D.E.S Solar Equipments Development Unit, BP386, Bou-Ismail, 42415, Wilaya of Tipaza, Algeria, EPST/CDER
[2]Advanced Electronics Laboratory (LEA), University of Batna, Avenue ChahidBoukhlouf, 05000, Batna, Algeria.

* Smail toufik.77@gmail.com

Presented in "2nd International Conference on Computational and Experimental Science and Engineering (ICCESEN-2015)"

Keywords
Analog to Digital Converter
current-mode.
current steering DAC
successive approximation ADC

Abstract: Nowadays the modeling is very important step in the integrated circuits design. For complex circuit architecture such as the Data Converter, in this paper, we developed new ideal model of 8-bit current-mode successive approximation analogue to digital converter (SAR-ADC). The proposed model is implemented in Matlab Simulink environment; the system is modeled by constructing a set of subsystems in SIMULINK environment with different blocks, non-ideal effects are not yet implemented, the main blocks of current-mode SAR ADC are a current sample and hold, a current comparator, SAR logic register and current steering digital to analogue converter (DAC). The simulation results with the static and dynamic performance, confirm the good performance and the high accuracy of the model.

1. Introduction

Due to the huge increase of the architecture and the complexity of mixed signal circuits, the use of behavioral model is necessary to design and simulate the performance of those circuits [1-2-3-4-5], Nowadays the modeling is very important step in the integrated circuits design. For complex circuit architecture such as the Data Converter, the modeling output helps the designer by confirming the performance characteristics of circuits and checking their electrical specifications; Modeling and simulation have increased the designer efficiency and ability to develop increasingly complex and useful electronic circuits, particularly at the integrated circuit (IC) level. Each type of circuit considered has its own particular requirements, in terms of design performance (specifications), design methodologies required to realize the design, modeling and simulation toolsets utilized, designer experience and skills set. Research in analog integrated circuits has recently gone in the direction of low-voltage (LV) , low-power (LP) design, especially in the environment of portable systems where a low supply voltage generated by a single-cell battery is used. These LV circuits have to show also a reduced power consumption to maintain a longer battery lifetime. In this area, traditional voltage mode techniques are going to be substituted by the current-mode approach. Selecting architecture is important since each analog-to-digital converter (ADC) architecture has specific advantages with respect to sampling rate, noise, resolution, dynamic range, power consumption, and implementation area [6]. The Successive approximation ADC (SAR ADC) has been known as a suitable low-power solution for many years [5]. The design of high-performance ADCs

presents difficult challenges as applications call for higher speed and resolutions, and as device dimensions and supply voltages are scaled down [7]. For this purpose the current-mode technique brought many solutions for compatibility with low power supply, high speed and small chip area. The SAR ADCs have received renewed attention due to their excellent power efficiency and low-voltage potential compared to pipelined and cyclic ADCs [6]. Since it does not require operational amplifiers, the voltage mode SAR ADC uses only a comparator and capacitors array in DAC circuit part. This raises two main issues; the first one is the need for large chip area and the second issue is the long settling time [5]. in the other part the Power consumption in the voltage SAR ADC is mainly from the DAC [8], For this reason, the current mode SAR ADC is designed with current source array serving in the DAC for decreasing the effect of long settling time and the power consumption. Moreover, No capacitors are used in the DAC and thus can be made very small compared to voltage SAR ADC [9].

In this paper, a new ideal model of the current-mode SAR ADC is introduced to predict the static and dynamic performance of this type of circuit. The main advantage of this behavioral modeling approach is that offer a low computing time and it is characterized by a less complexity of design in comparing to level transistor method. The proposed model is implemented in the popular Matlab Simulink environment, non-ideal effects are not yet implemented and only basic functionality is checked, These model are implemented by using elementary Simulink of library blocks with take in consideration the computational cost is minimum as possible. The current mode SAR ADC consists of current-mode block such as current Sample and Hold, a current comparator, a current steering DAC and SAR logic register [5].

This paper is organized as the flowing; after the introduction, the behavioral model of SAR ADC is presented in the second section. The different parts of the model are reported in the third section of the paper. Finally, Simulation results and conclusion can be found in the fourth and the fifth sections respectively.

2. The ADC architecture

The block diagram of current mode SAR ADC architecture is shown in Fig. 1. The current steering DAC is the critical building block of the current mode SAR ADC. The operation principle of this current mode SAR ADC is similar to the conventional voltage mode SAR ADC [5]. However, current-mode converters are now demonstrating excellent characteristics and in particular, high resources efficiency (power and area) [10]. The ADC works by using a DAC and comparator to perform a binary search to find the input voltage. A sample and hold circuit (S&H) is used to sample the analog input and hold the sampled value whilst the binary search is performed. The binary search starts with the Most Significant Bit (MSB) and works towards the Least Significant Bit (LSB). For a 8-bit output resolution [11], and in contrast to voltage mode, the current mode ADC uses only CMOS transistor in the DAC as current sources and logical operation. This has the advantage to reduce the area requirements, reduce power consumption and achieve high speed operation [10].

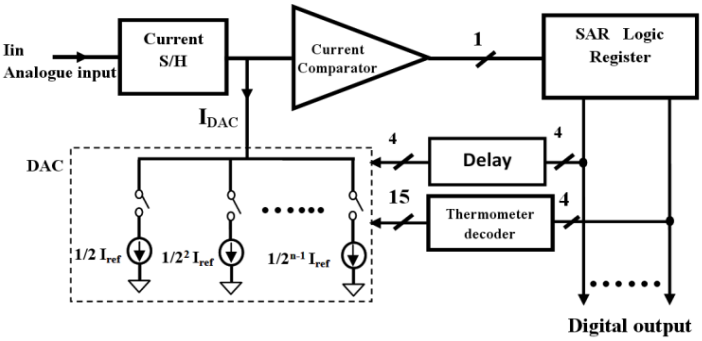

Figure1. *Current mode SAR ADC architecture*

3. Simulink behavioral model of SAR ADC

Simulink model of current mode SAR ADC is shown in Fig 2. It consists of five major blocks; a current S&H, a current comparator, a SAR logic register, a thermometer decoder, and 8-bit current steering DAC with 4 MSB and 4 LSB

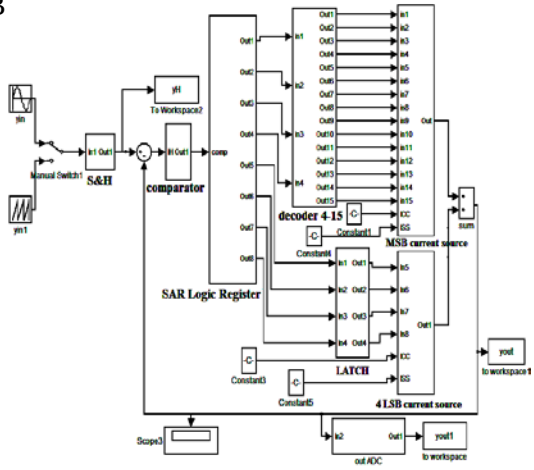

Figure2*.Simulink model ideal of current mode SAR ADC*

As shown in Fig. 3, the basic functionality of a current-mode SAR ADC is similar to voltage mode SAR ADC. The analog input current Iin is sampled by the S&H, the current comparator generate binary bits by the comparing the values of the S&H with the output of the current DAC. To implement the binary search algorithm, the N-bit register is first set to midscale, this is done by setting the MSB to '1' and all other bits to '0'. This forces the DAC output current IDAC to be half of the reference current IREF (IDAC = IREF/2). The S&H current I S/H is then compared with the IDAC. If IS/H is greater than IDAC, the comparator output is logic 1 and the MSB of the N-bit register remains at 1. Conversely, if IS/H is less than IDAC the comparator output is logic 0 and the MSB of the register is changed to 0. Then, the SAR control logic moves to the next bit down, forces that bit high, and does another comparison. The sequence continues all the way down to the LSB. Once this is done, the conversion is completed, and the N-bit digital word is available in the register.

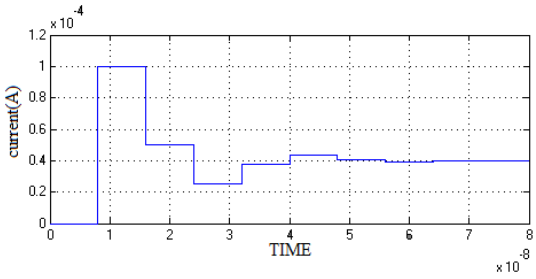

***Figure3**. 8-bit Current mode SAR ADC operation*

3.1. Sample and hold model

ADCs employ a S&H circuit in front end to achieve high precision, linearity and dynamic range [11].The S&H samples the analogue input signal and holds the value for certain time, the model ideal of the sample and hold is shown in Fig. 4.

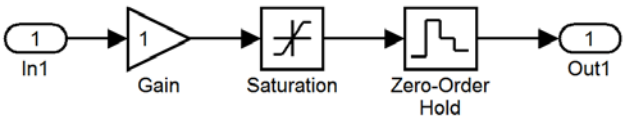

***Figure4**. Sample and Hold model*

3.2. Comparator model

The comparator is a key component of the data converter as it is the link between the analogue and digital domain [12]. In the comparator model as shown in Fig. 5, the input is the subtraction between the output of the S&H and the DAC. On the top of this, a constant value is added to this subtraction to model the offset of the real comparator (in the ideal case the value of the offset is zero). The result is then multiplied by a gain that represents the amplification stage. Then the result is saturated to full logic levels and compared to zero to define which of the two inputs the highest one is.

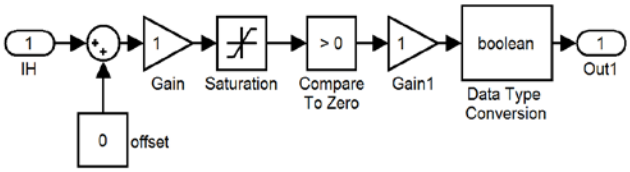

***Figure5**. Comparator model*

3.3. SAR Logic Register

The SAR logic Register is the heart of the system. It generates the controls signal used by the current steering DAC. The logic block (as shown in Fig. 6) has been implemented using two shift registers in order to perform the successive approximation routine. Each shift register is composed of a chain of nine D Flip-Flops. The shift register on the top is used as a sequencer and is synchronous with the internal clock. The bottom register stores the conversion value. Each sampled value (sampling is performed by S&H) of the analogue signal current input is compared by the current comparator with the output of the current DAC. The result of the comparison is used then by the SAR to elaborate the next step.

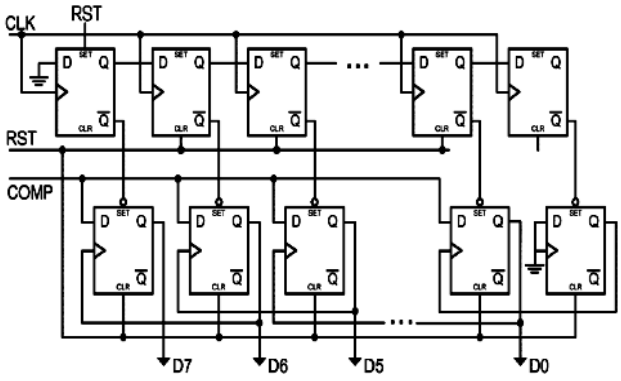

***Figure6**. SAR logic register.*

4-bit binary inputs are converted to 15-bit thermometer codes by the mean of a 4-to-15 binary-to-thermometer decoder, this decoder is constructed by using OR and

AND gates available in SIMULINK library. The decoder is shown in Fig. 7

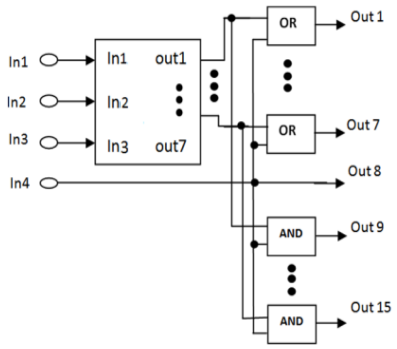

Figure7. *4 to 15 binary thermometer decoder*

3.4. The current steering DAC

The current steering DAC is suitable for high speed and high resolution application [13]. Fig. 8 shows the overall structure of the 8-bit current-steering DAC. The 8-bit input binary data is segmented into the 4 most significant bits (MSBs) and 4 least significant (LSBs), for 4 MSBs bits are decoded by the thermometer in order to control 15 identical current sources, such as the first MSB bit control 23 current source, the second MSB bit control 22 current sources, the third MSB bit control 21 current sources, and the fourth MSB bit control 20 current sources, and 4 least significant (LSBs) are directly applied to the 4 current sources.

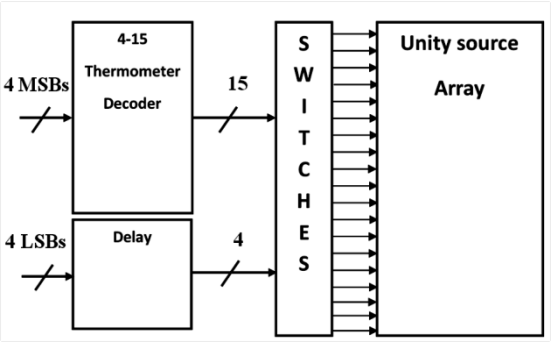

Figure8*. General structure of the 8-bit current-steering DAC*

In the DAC model, each current source is multiplied by gain factor in such a way it became equal to the current source value, the model of switches and current sources array controlled from 4 MSBs, the model of DAC for 4 LSB it is shown in Fig 9.

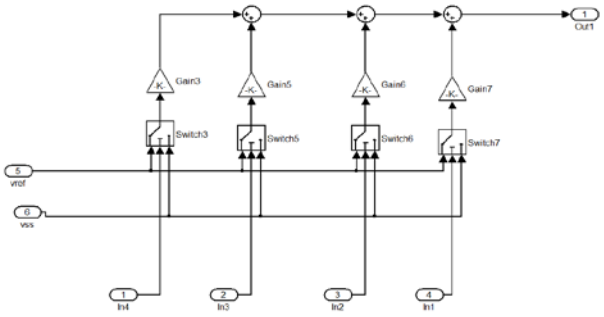

Figure9. *Model of switches and current sources.*

4. Simulation results

To check and to confirm the performance of the new proposed model, simulation is performed and its results are reported in this section with the static and the dynamic performances.

4.1. Dynamic performance

In order to test the ideal model and to confirm its dynamic performance, an analogue signal equivalent to a sine wave with a frequency of 63 KHz is applied to the input of the ADC with sampling rate of 5 MHz as shown in Figure 10. Simulation results of the output signal from the DAC and reconstructed analog signal from ADC are shown in Fig 11 and 12.

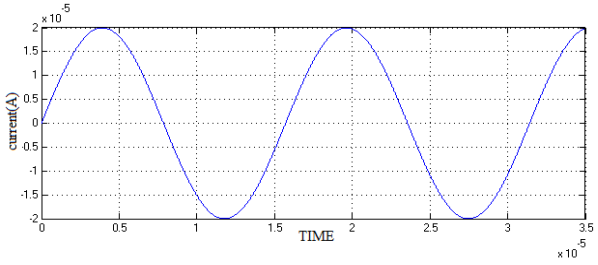

Figure10*. The analogue input signal*

The dynamic performance including Signal to Noise Ratio (SNR), Spurious-Free Dynamic Range (SFDR) and Total Harmonic Distortion (THD). By using the Fast Fourier

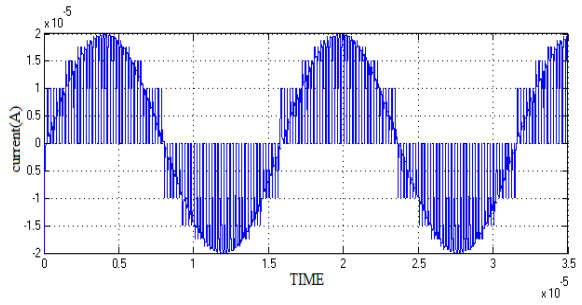

***Figure11**. The analogue signal output from the DAC*

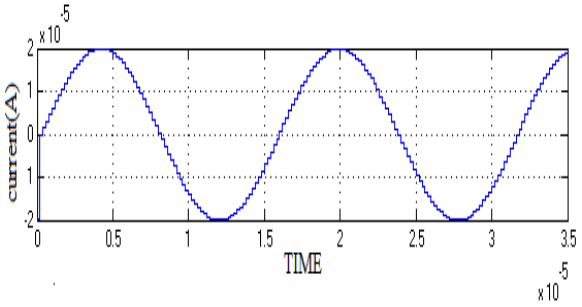

***Figure12**. The analogue signal reconstructed from the output of the ADC*

Transform (FFT), the SFDR and THD can be calculated from the power spectrum. The FFT of the output signal for an ideal model of current mode SAR ADC is shown in Fig13. For the ideal model we extracted a SNR is 49.92dB, The SFDR is 66 dB and the effective number of bits is ENOB=7.9dB.

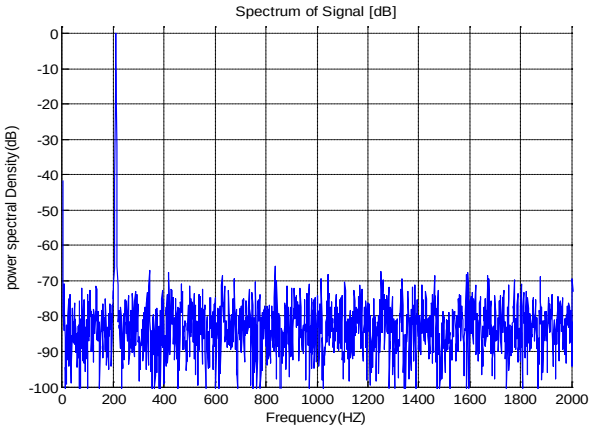

***Figure13**. FFT of the ADC output signal in the ideal case with Fin = 63 kHz; Fs = 12.5MHz*

4.2. Static performance

The linearity is the most important parameter in the data converter. The linearity performance includes Integral Non-Linearity (INL) and Differential Non-Linearity (DNL). The INL is defined as the maximum deviation of a transition point of a conversion from corresponding transition point of an ideal conversion. The INL is simulated using a MATLAB code. Based on INL definition, the LSB will be the deviation of the real transfer function from a straight line. For the DNL, it is defined as the difference between an actual step width and the ideal value of 1LSB. Hence, INL will represent cumulative DNL errors. The DNL is simulated using MATLAB code based by this equation:

$$INL_J = \sum_{i=1}^{j-1} DNL_J$$

The simulation results of DNL and INL are shown in Fig 14 and 15 respectively. The results are of a 8-bit current mode SAR ADC for ideal model. The simulation results show that the variation of the DNL and INL is more or less around 1LSB, it is between +0.14/-0.13 LSB for DNL, and for INL it is in the range of INLmax of +0.35 LSB and INLmin of -0.35 LSB.

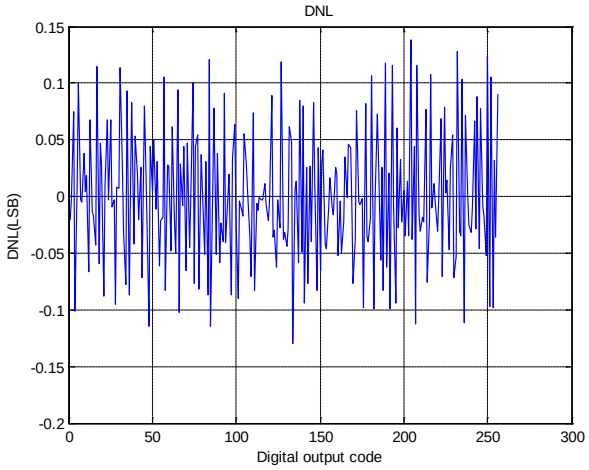

***Figure14** DNL of the ideal 8 bit current mode SAR ADC*

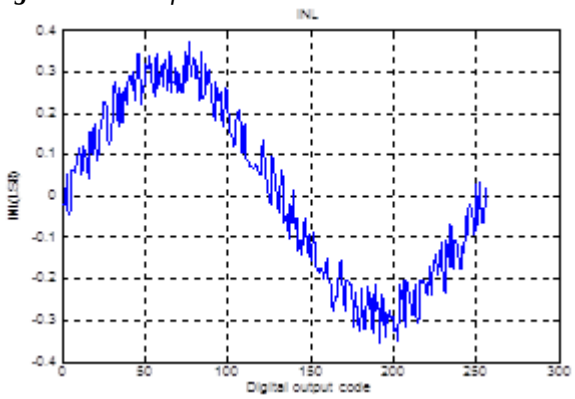

***Figure15**. INL of the ideal 8 bit current mode SAR ADC*

From the results presented in the previous section we can comparison between our behavioral ideal ADC model, and real ADCs with current and analogue mode [5-14-15] can be seen in Table 1. There is a good match between the proposed models and the real ADCs with

current and voltage mode, this proves the accuracy of our behavior model.

Table 1 Comparison the Performance of the current mode SAR ADC MODEL.

Parameters	This work/ Ideal model	[5]	[14]	[15]
VDD	1V	1.2v	1.4v	1.8v
Mode	I-Mode	I-Mode	voltage mode	voltage mode
Resolution (bit)	8	8	8	10
INL (LSB)	-0.35/0.35	-0,56/0:9	-0.2/0.27	-1.02/0.824
DNL (LSB)	-0.13/0.14	-0,84/1:0	-0.18/0.34	-0.2/0.6
SNR (dB)	49.25	/	/	/
SFDR (dB)	65.3	61.64	/	72.025
SNDR (dB)	49.2	46.2	48.2	60.55
ENOB (bit)	7.9	7.38	7.8	9.767

5. Conclusions

A new model of ideal 8-bit current mode SAR ADC has been reported. The analogue blocks are modeled in ideal case. For current comparator, it has been modeled by taking into account that the offset and the delay time of the comparator are equal to zero. For sample and hold, the effect of the charge injection, clock feedthrough, clock jitter and the switching noise have been neglected in this work. The analysis of static and dynamic performances using MATLAB environment confirm the good performance of the model. The behavioral model and the simulation results will help the designer to achieve 8-bit current mode SAR ADC circuit with a low power, a current range in the scale of µA and high efficiency in the chip area by using steering current DAC.

References

[1] Samir Barra, Abdelghani Dendouga, Souhil Kouda, and Nour-Eddine Bouguechal, "Contribution to the Analysis and Modeling of the Non Ideal Effects of Pipelined ADCs using MATLAB", Journal of Circuits Systems and Computers, vol. 22, no. 2, Feb. 2013.

[2] J. Ruiz-Amaya, M. Delgado-Restituto, A. Rodrguez-Vazquez, “Behavioral modeling of pipeline ADC building blocks”, International Journal of Circuit Theory and Applications, vol. 40, no. 6, pp. 571-594, 2012.

[3] A. Dendouga, N. E. Bouguechal, S. Kouda, S. Barra, B. Lakehal, “Contribution to the modeling of a non-ideal Sigma-delta modulator”, Journal of Computational Electronics, vol. 11, no. 4, pp. 321-329, 2012.

[4] Piero Malcovati, Simona Brigati, Fabrizio Francesconi, Franco Maloberti, Paolo Cusinato and Andrea Baschirotto, “behavioral modeling of switched-capacitor sigma–delta modulators”, IEEE Transactions on Circuits and Systems - fundamental theory and applications, vol. 50, no. 3, march 2003.

[5] Xian Tang and Kong Pang Pun, A Novel Switched-Current Successive Approximation ADC, Journal of Circuits Systems, and Computers, 2011, vol. 20, no. 1, pp.15_27.

[6] Ying-Zu Lin, Chun-Cheng Liu, Guan-Ying Huang, A 9-Bit 150-MS/s Subrange ADC Based on SAR Architecture in 90-nm CMOS, IEEE Transactions on Circuits and Systems-I, vol. 60, no. 3, pp. 570–581, March 2013.

[7] Neena Nambiar, Benjamin J. Blalock and M. Nance Ericson, “A novel current-mode multi-channel integrating ADC”, Analog Integr Circ Sig Process, vol. 63, pp.283–291, 2010.

[8] Weibo Hu, Donald Y.C. Lie, and Yen-Ting Liu, “An 8-bit Single-Ended Ultra-Low-Power SAR ADC with a Novel DAC Switching Method”, IEEE Transactions on Circuits and Systems-I, vol. 60, no. 7, pp. 1726–1739, July 2013.

[9] Bard Haaheim_y and Timothy G. Constandinou, “A sub-1_W, 16kHz Current-Mode SAR-ADC for Single-Neuron Spike Recording”, in the proceeding of IEEE International Symposium on Circuit And Systems (ISCAS), 2012.

[10] S. Heydarzadeh, A. Kadivarian, and P. Torkzadeh, “Implemented 5-bit 125-MS/s Successive Approximation Register ADC on FPGA”, World Academy of Science, Engineering and Technology, vol. 69, pp. 394-397, 2012.

[11] R. Dlugosz and K. Iniewski, “Flexible architecture of ultra-low-power current-mode interleaved successive approximation analog-to-digital converter for wireless sensor networks”, VLSI Design, vol. 2007, no. 2, pp.1–13, 2007.

[12] Daniela DeVenuto, David Tio Castro, Youri Ponomarev, and Eduard Stikvoort, “0.8 mW 12-bitSAR ADC sensors interface for RFID applications”, Microelectronics Journal, vol.41, pp.746–751, 2010.

[13] Indrit Myderrizi, and Ali Zeki, “Behavioral Model of Segmented Current-Steering DAC by Using SIMULINK”, in the proceeding of Ph.D Research in Microelectronics and Electronics, , pp.156 – 159, 2009.

[14] Weibo Hu, Donald Y.C. Lie, and Yen-Ting Liu, An 8-bit Single-Ended Ultra-Low-Power SAR ADC with a Novel DAC Switching Method Vol. 4, NO. 3, pp. 17-22, Jan.-March issue (2011) , Journal on Electrical Engineering, special issue on “VLSI Design Methodologies/Embedded Systems”.

[15] Chung-Yi Li, Chih-Wen Lu, Hao-Tsun Chao, Chin Hsia ,A 10-Bit Area-Efficient SAR ADC with Re-usable Capacitive Array, The sixth IEEE International Conference on Anti-counterfeiting, Security, and Identification , 24-26 August

International Journal of Computational and Experimental Science and Engineering (IJCESEN)
Vol. 1-No.2 (2015) pp. 7-11
http://dergipark.ulakbim.gov.tr/ijcesen

ISSN: **2149-9144**

Research Article

Comparative study of etching silicon wafers with NaOH and KOH solutions[#]

M.MAOUDJ[1,2*], D.BOUHAFS[1], N.BOUROUBA[2], R. BOUFNİK[1], A.El AMRANİ[1], A.Hamida FERHAT[2]

[1]CRTSE, Division Développement des Dispositifs de Conversion à Semi-conducteurs, 02 Bd Frantz Fanon, BP 140 Alger 7- merveilles, Algiers, Algeria
[2] University Ferhat Abbas, Faculty of Technology, Department of Electronics, Setif, Algeria.

* Corresponding Author : maomo72@yahoo.fr
[#] Presented in "2nd International Conference on Computational and Experimental Science and Engineering (ICCESEN-2015)"

Keywords
Surface morphology
Surface passivation
Carrier lifetime
Optical reflection

Abstract: In this study, we investigated the effects of alkaline post-etching surface morphology on minority carrier lifetime of the p-type monocrystalline silicon wafers. A Sodium hydroxide and potassium hydroxide solutions at 30% and 23%, respectively, have been used at constant temperature. The surface states were characterized by calculation of the arithmetical average roughness (Ra) and the UV–visible-NIR optical reflectivity, whereas, the electrical characterization was done by means of quasi-steady state photoconductance measurements, which revealed a correlation between the resulted surface state and the minority carrier lifetime. The Measured surface roughness shown that potassium hydroxide solutions at 23% by weight gave a high minority carriers lifetime.

1. Introduction

M With the extraordinary increasing performance of electronic devices, the influence of the surface states of silicon wafers is becoming paramount for a highly competitive industry in the field of semiconductors in general and Photovoltaic (PV) in particular. Currently, the chemical treatments of silicon substrate surface represent a capital step in PV technology. They are used to improve electrical and optical properties of devices [1].
Indeed, the surface of silicon wafers is an important source of charge carriers recombination due to the presence of several crystalline defects among which the discontinuity of the crystal lattice is the most important. The density of these defects are expressed as a density of interface states, which in statistical Shokley-Read-Hall (SRH), are characterized by their energy levels in the band gap and their capture cross section (σ_n, σ_p) [2-3-4] .
However, this surface carriers recombination centers will mainly affect the device electrical performance. So, to reduce the surface recombination, we must have firstly a good surface in terms of dangling bonds and roughness. In their works Shui-Yang Lien et al. [5], have shown that there is a dependency between the surface condition and the lifetime of the minority carriers.
In this work, we investigate the effects of surface morphology on silicon wafer minority carrier lifetime by utilization of two alkaline solutions, KOH and NaOH. To identify the KOH solution providing the smoothest Si surface, in the first step, we optimize the KOH solution by investigating four different concentrations at a constant temperature of 90 °C. In the second step, we compared the results of the optimized KOH solution in terms of surface states which obtained with the usual solution of NaOH 30% by weight. Finally, a correlation between the surface states and the lifetime of the minority carriers was investigated.

2 Experimental

The etching experiments were carried out on p-type boron doped <100> oriented Cz-monocrystalline silicon (c-Si), with a thickness of about 420 µm and resistivity of 1–3 Ω cm. After a conventional cleaning process, the double sided thinning and polishing of silicon substrates was done in several KOH bath at a constant temperature, to reach a final thickness of 320 µm. The concentrations investigated are 15%, 23%, 30% and 40%. The aim of this study is firstly, to determine the KOH concentrations which shows the smoothest etched silicon surface and then the optimum of KOH concentration obtained in term of low surface roughness, is compared with surfaces obtained by NaOH bath prepared at 30% by weight, which is widely refer in several works. So, it is important to note that each silicon substrate is etched in a freshly prepared alkaline hydroxides solution. The polishing bath was maintained at a constant temperature of 90 °C for KOH bath and 100 °C for NaOH.

A continuous nitrogen gas bubbling was introduced in the solution from the bottom of the polishing bath to keep the solution composition and temperature uniform. After polishing, the wafers were rinsed in DI water for 5min and then dried by nitrogen flow [6].

The quality of the etched surfaces was inspected using a calculation of the arithmetical average roughness (Ra), using TESA-RUGO Surf roughness depth measuring equipment, with a course of 5 µm and the UV–visible-NIR optical reflectivity using Carry 500 spectrophotometer.

The Carry 500 spectrophotometer is a dual beam system with a spectral range extending from 175 to 3300 nm [7].

The correlation between the surfaces treated with the two different alkaline hydroxides solution and the carriers lifetime was highlighted by Quasi-Steady State Photo-Conductance (QSSPC) measurement, which was performed by SINTON WCT-120 tester, these measurements allow the determination of the injection level dependent minority carrier lifetime [5].

3 Results and Discussion

3.1 Surface analysis

3.1.1 Evaluation of roughness for optimum KOH concentration

The surface Roughness of the KOH solution for varying concentrations was experimentally determined and plotted as shown in Figure 1. The roughness of the different surfaces can be calculated as an arithmetical average roughness Ra [8]:

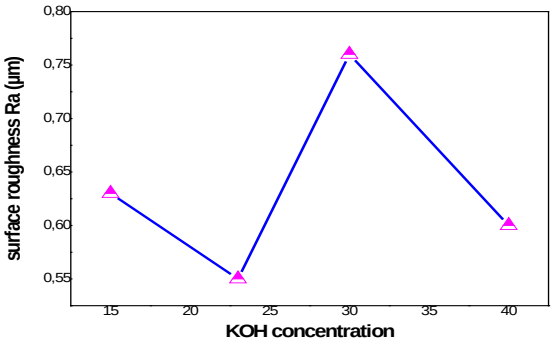

Fig.1 Influence of KOH concentration on roughness of <100> silicon (Etchant: 90°C-KOH)

Figure 1 shows the influence of KOH concentration on the surface roughness of the wafers etched for 20 minutes at a constant temperature of 90 °C, we compared the roughness of <100> silicon wafers etched by KOH-water solutions of four different KOH concentrations, 15% wt., 23% wt., 30% wt. and 40% wt.

K. Sato et al. shows in their work, that the roughness decreases with an increase in KOH concentration on <110> silicon [9]. But in our study, after several tests on several samples, we found that there is no linearity between KOH concentration and the roughness on <100> silicon.

From Figure 1, we observed that the roughness of less than 0.55 µm in Ra was achieved under the condition of 23% wt. KOH concentration, when the etching depth was about 100 µm.

For the other measurements of Ra at different KOH concentration, we found:

Ra (15%) = 0.63 µm, Ra (30%) = 0.76 µm and Ra (40%) = 0.60 µm. In conclusion we can say that the concentration of 23% represents the concentration which gave the best surface roughness.

Marvell Nanofabrication Laboratory of the University of California, Berkley, found the same results, and report in their lab manual that 24% by volume KOH etch rate is the fastest and shows the smoothest etched Si surface on <100> p-type Si wafers at a temperature of 80 °C [10].

3.1.2 Surface reflectivity

To confirm the tests undertaken previously, we studied the surface reflectivity by a spectrophotometer, and the weighted reflectance was evaluated.

It's widely known that, reflection off of smooth surfaces such as mirrors leads to a type of reflection known as specular reflection.

Reflection off of rough surfaces leads to a type of reflection known as diffuse reflection. Whether, the surface is microscopically rough or smooth has a tremendous impact upon the subsequent reflection of a beam of light. The diagram below depicts two beams of light incident upon a rough and a smooth surface [11].

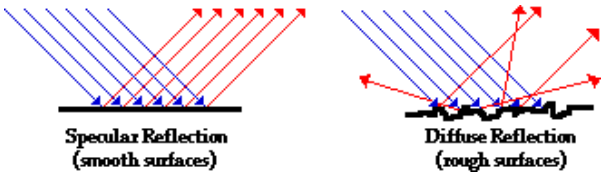

Fig.2 Different type of reflection on solid surface

From these above definitions, we can write the empirical equation for the total reflection:

$$R_{tot} = R_{diffuse} + R_{specular} \quad (1)$$

This equation has the consequence that, for low surface roughness, the diffuse reflection tends to zero; this result was used for the surfaces characterization, of our samples.

As depicted in Figure 3 the reference sample (pink curve) which represents poly-optical silicon wafer, the reflection is a specular type (mirror surface), and thus, the diffuse reflection is practically equal to zero. By comparison of the absorption spectrum of the reference sample and the other absorption spectra of different samples, as shown in Figure 3, we can notice that the reflectivity can be affected by the solution concentration for a fixed etching duration and temperature; because the reflectivity is related to the surface quality which is related to the concentration of hydroxide etchant solution.

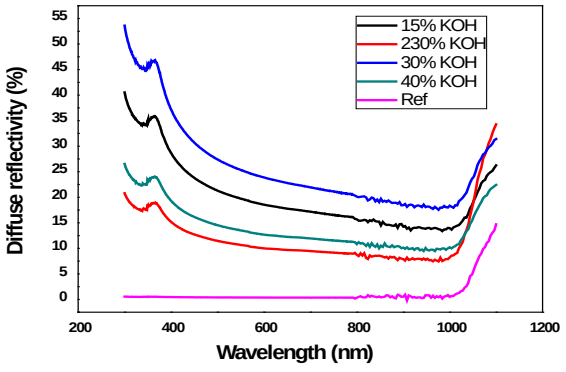

Fig.3 Reflectivity of c-Si surface polished with different KOH concentration

Moreover, Figure 3 shows a perfect correlation between the arithmetical average roughness calculation and reflectance results. We can see on the diagram of reflectivity, that the reflection of the surface which was treated by 23% KOH concentration displayed the lowest reflection than the better surface in term of roughness; this result is well confirmed by its Ra which is equal to 0.55 µm, such results remains valid for the other concentration of KOH, the correlation between the arithmetical average roughness and the surface reflectance represented by the weighted reflection is shown in the following Table.

Table 1. Correlation between arithmetical average roughness and weighted reflection at different concentration of KOH solution.

KOH concentration	Ra (µm)	Weighted reflectance
15% wt.	0.63	19.25%
23% wt.	0.55	10.84%
30 % wt.	0.76	23.95%
40 % wt.	0.60	13.03%

It is quite clear from the table above that, for the lower value of Ra (µm) we have the lowest value of the weighted reflectance and then, for the highest value of Ra (µm), we have also the highest value of the weighted reflection. This is also valid for intermediate values.

3.1.2 Comparison of Surface treatments by KOH 23% wt. and NaOH 30% wt.

In this section, we conducted the same study that previously, the figure 4 represents the reflectivity of c-Si surface polished with KOH 23% wt solution and NaOH 30% wt.

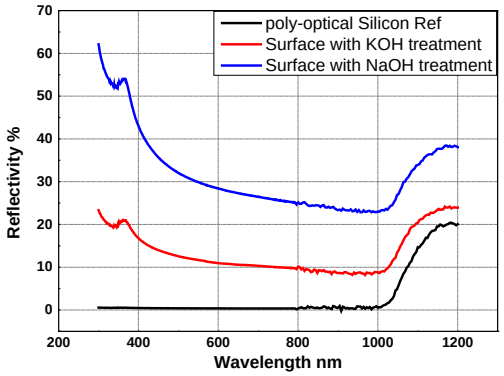

Fig.4 Reflectivity of c-Si surface polished with KOH 23% wt solution and NaOH 30% wt solution

The results obtained from the figure 4 in terms of weighted reflectance and roughness calculation of the two different polishing processes are listed in Table 2.

Table 2. Overview over results obtained for NaOH and KOH surface treatment.

Chemical solution	Ra (µm)	Weighted reflectance
KOH 23% wt. - 90°C	0.55	10.84%
NaOH 30% wt.- 100°C	0.73	28.5%

According to these results, it is clear that the KOH polishing gives the best results in terms of surface quality comparing to the results obtained by NaOH treatment.
The optical weighted reflection (Rw) of KOH treatment is the lowest value of 10.84%, and the Rw value of NaOH treatment is about 28.5%. This value is higher comparing to the KOH results. These results are confirmed by the Arithmetical average roughness calculation Ra represented on table 2.

4. Impact of the surface quality treated with optimized NaOH and KOH solution on electrical properties of silicon wafers

4.1 Minority carrier lifetime evaluation

The minority carrier lifetime (τ_{app}) is measured using the Sinton WCT-120 lifetime tester in generalized Quasi-Steady-State Photoconductance (QSSPC) mode. The measurements are carried out on silicon substrates treated with KOH at 23% by weight concentration and NaOH at 30% weight concentration.
The impact of polishing by KOH and NaOH solution and resultant surface quality on carrier lifetime is investigated. The results obtained by QSSPC measurements are presented in Figures 4, which shows the dependence of the apparent lifetime on the injection level of the two surfaces treated respectively by 23% wt. KOH and 30% wt. NaOH before and after Iodine-Ethanol passivation.

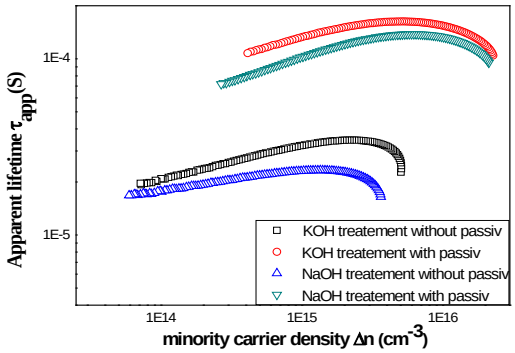

Fig.4 Apparent lifetime vs. minority excess carrier

It can be seen as depicted in Figure 4, and by the comparison of the two surfaces states, that, the roughest surface presents the weakest carrier lifetime, while the smoothest surface gives the highest lifetime. The experimental values of carrier lifetime of the two surfaces which treated by KOH and NaOH are respectively, τ_{app}(NaOH) = 101.6 µs and τ_{app}(KOH) = 132 µs with Iodine-Ethanol surface passivation, and τ_{app}(NaOH) = 23 µs, However, τ_{app}(KOH) = 32 µs without Iodine-Ethanol surface passivation at the injection level $\Delta n = 1.10^{15}$ cm^{-3}.
In any case, we note that the surfaces treated with 23% KOH represents the best results in terms of carrier lifetime, it seems to be clear that the enhancement between these results is closely related to the surface treatment.
This result could be related to increased surface defect states due to expanded surface area, this would involve additional dangling bonds and therefore increases the surface recombination velocity, leading to a decrease of the measured τ_{app} [12, 13]. Always from Figure 5, we can deduce that the effect of traps is negligible in Cz-silicon samples, because the trapping leads to an increasing apparent in lifetime with decreasing injection density [7].

Conclusion

An investigation of the surface state of silicon after alkali solution polishing has been presented. Several alkaline based wet chemical etching sequences are tested in terms of resulting surface roughness, electrical and optical performance. All the flatness parameters obtained from our analysis clearly indicate the superiority of the KOH polishing process as compared to NaOH polishing.

Our study also reveals that the KOH thinning-polishing at 23% by weight concentration process gives the smoothest surface comparing with the NaOH treatment and KOH treatment gives also the lowest reflection is a controlled, this different parameters was correlated to electrical properties in terms of carrier lifetime. In conclusion, the aim of our study is to enhance the minority lifetime of the wafer by modifying its surface roughness.

Acknowledgement

This work is realized at the DDCS-Division/CRTSE and financed by the National Fund for Research of Algeria – DGRSDT/MESRS.

References

[1] De A. Baudrant, François Tardif, Christophe Wyon, Book « Caractérisation et nettoyage du silicium », édition Lavoisier 2003, ISBN 2-7462-0605-6.

[2] T. Di Gilio, Thesis ”Etude de la fiabilité porteurs chauds et des performances des technologies CMOS 0.13 µm - 2nm,”, Institut Supérieur de l’Electronique et du Numérique (ISEN), Toulon, France, 2006.

[3] A.Bentzen, Thesis: “Phosphorus diffusion and gettering in silicon solar cells”, university of oslo, October 2006.

[4] Ji Youn Lee, Thesis “Rapid Thermal Processing of Silicon Solar Cells Passivation and Diffusion”, Albert-Ludwigs-University of Freiburg, 2003.

[5] Shui-Yang Lien et al, “Influence of Surface Morphology on the Effective Lifetime and performance of Silicon Heterojunction Solar Cell”, International journal of photoenergy volume, article ID 273615, 2015.

[6] P.K. Basu et al. “A cost-effective alkaline multicrystalline silicon surface polishing solution with improved smoothness”, Solar Energy Materials & Solar Cells 93 (2009), pp 1743–1748.

[7] Information found on http://www.crtse.dz/media/moyens/caracterisation/ Spectrophotometre-IR-Thermo-Nicolet.pdf.

[8] J. Rentsch et al. “Single side etching – key technology for industrial high efficiency processing”, 23rd European Photovoltaic Solar Energy Conference, 1-5 September 2008, Valencia, Spain.

[9] Kazuo Sato et al. “Roughening of single-crystal silicon surface etched by KOH water solution”, Elsevier, sensor and actuators 73 (1999), pp 122-130.

[10] Information found on: https://nanolab.berkeley.edu/labmanual/chap2/2.04msink4.pdf.

[11] Information found on: http://www.physicsclassroom.com/class/refln/Lesson-1/Specular-vs-Diffuse-Reflection.

[12] H.Park et al, “Improvement on surface texturing of single crystalline silicon for solar cells by saw-damage etching using an acidic solution”, Solar Energy Materials & Solar Cells 93 (2009), pp 1773–1778.

[13] H. Yan et al., “Influence of annealing and interfacial roughness on the performance of bilayer donor/acceptor polymer photovoltaic devices,” Advanced Functional Materials, vol. 20, (2010), pp. 4329–4337.

International Journal of Computational and Experimental Science and Engineering (IJCESEN)
Vol. 1-No.2 (2015) pp. 12-15
http://dergipark.ulakbim.gov.tr/ijcesen

ISSN: **2149-9144**

Research Article

Analysis of Canadian Armed Forces CH149 Aircraft Replacement/Overhaul Options[#]

Ahmed GHANMI[1]*, Gregory VAN BAVEL[2]

[1,2] Defence Research and Development Canada, Centre for Operational Research and Analysis
Ottawa, Ontario, K1A 0K2, Canada

* Corresponding Author : ahmed.ghanmi@forces.gc.ca

[#] Presented in "2nd International Conference on Computational and Experimental Science and Engineering (ICCESEN-2015)"

Keywords
Aircraft
Cost
Maintenance
Military

Abstract: Aging aircraft present significant technical, economical, and operational challenges for military decision makers. As aircraft mature beyond their planned service lives, their maintenance needs may become less predictable and their overall operational availability tends to decrease. Operations and Maintenance (O&M) costs normally increase over time and eventually become prohibitive, thereby providing strong evidence that the aircraft should be replaced. This paper presents an analysis of the Canadian Armed Forces CH149 aircraft replacement and overhaul options. The analysis identified three potential decision regions for the aircraft replace/lease/upgrade options, depending on the O&M cost reduction factor and the lease cost. Sensitivity and risk analyses were conducted to assess the impact of key parameters on the decision regions.

1. Introduction

Aging aircraft present significant technical, economical, and operational challenges for military decision makers. As aircraft mature beyond their planned service lives, their maintenance needs may become less predictable. Corrosion, for example, may require additional inspections and repairs. Aircraft may also become less resilient with age, so that random events pose increasingly serious maintenance challenges. As aircraft age, it is expected that increasing Operations and Maintenance (O&M) costs will eventually become prohibitive, thereby suggesting that the aircraft should be replaced. From an operational perspective, the overall operational availability (Ao) of military aircraft tends to decrease with age. Ao is an important consideration in the evaluation of system performance, readiness, and sustainability.

This paper presents an analysis of the Canadian Armed Forces CH149 aircraft replacement/ overhaul options. The CH149 Cormorant is Canada's primary search-and-rescue (SAR) helicopter. Since delivery, the CH149 fleet has not reached its Ao target set in the original statement of requirements. In addition to lower than expected Ao, the O&M costs of the CH149 fleet have increased significantly over the past few years. Various unanticipated maintenance problems, such as early on-set corrosion, have contributed to degraded performance and upwardly spiralling O&M costs.

A simulation-based economic model was developed to assess the cost effectiveness of the CH149 replacement/ overhaul options [1]. The model used the Geometric Brownian Motion (GBM) [2] method to forecast the aircraft O&M cost trends and applied cost comparison methods of engineering economics [3] to assess the cost effectiveness of the CH149 replacement/ overhaul options. GBM is a continuous-time stochastic process in which the logarithm of the randomly varying quantity follows a Brownian motion with drift. GBM accommodates random events through a diffusion process and upward trends through a drift process. Three proposed aircraft replacement and overhaul options (Upgrade, Lease, and Replace) were investigated.

The Upgrade option considers upgrading the current CH149 fleet (14 aircraft) and expanding it with six additional (new) aircraft. It is assumed that upgrading the current CH149 aircraft would reduce their O&M costs by a factor called the O&M cost reduction factor. The Lease option considers replacing the current CH149 fleet with 20 leased aircraft of similar operational capabilities for a fixed annual cost called the lease cost. The Replace option considers replacing the current CH149 fleet with 20 new aircraft of similar capabilities. For simplicity, it is assumed that 10 aircraft will be delivered at the beginning of the project and the remaining 10 aircraft will be delivered five years later. In this case, the current CH149 fleet would remain in service until the delivery of the last aircraft.

2. O&M Cost Process

To assess the cost effectiveness of the aircraft replacement/ overhaul options, historical O&M costs of the current CH149 fleet were collected and analysed. A data set of ten annual O&M costs per aircraft for the years 2003 to 2012 was obtained from the Defence Financial Management Accounting System: 0.677, 1.623, 2.269, 2.422, 3.746, 5.559, 4.885, 5.811, 7.509, 8.030 ($M). The first step in the analysis is to test the GBM model assumptions using the data sample. There are a number of theoretical goodness-of-fit tests that can be applied for small samples, and the two of the best known distance tests are Anderson-Darling and Lilliefors [4]. The application of these tests to the O&M cost data gave a p-value of 0.59 for Anderson-Darling and 0.50 for Lilliefors, indicating a failure to reject the null hypothesis that the sample comes from a normal distribution at a significance level of 5%. To test the data for the independence assumption, the sample autocorrelation function (ACF) of the data was calculated and compared with the theoretical ACF derived from the GBM process. The test indicates that most of the data is confined to the 95% confidence bands of the autocorrelation function, except for lags 1 and 2. At lags larger than 2, the sample ACF becomes consistent with white noise.

Using the maximum likelihood technique, the GBM model parameters (mean and standard deviation) are estimated from the O&M cost data as: $\mu = 0.25$ per year and $\sigma = 0.27$ per year1/2. Figure 1 depicts the CH149 O&M cost data and projected sample paths generated using the GBM model. The contour denotes the boundary that contains 95% confidence interval for forecasted paths using the model parameters.

3. Cost Effectiveness Analysis

The next step in the analysis is to use the economic model developed in [1] to determine the cost effective option for the CH149 replacement and overhaul. For the purpose of this paper, it is assumed that the O&M costs of the additional fleet, leased fleet and new fleet follow the same patterns (i.e., same GBM parameters) as the O&M costs of the current fleet. They are estimated by projecting the CH149 O&M cost data over time for different fleet sizes. It is also assumed that the O&M cost of a leased aircraft is higher than the O&M costs of a new aircraft by about 10% to 15% (for example). Given the lack of data, a set of hypothetical economic parameters for both the current and the new aircraft fleets was considered in the analysis. The details of the economic parameters (e.g., upgrade cost, book value of the aircraft, discount rate, etc.) can be found in [1]. Probability distributions (e.g., Program Evaluation and Review Technique) were used to represent the variability in these parameters and Monte Carlo simulation was applied to determine the expected costs of the aircraft replacement/overhaul options. The O&M cost reduction factor and the annual lease cost were used as decision variables in the study.

Figure 2 depicts three potential decision regions (Upgrade, Lease, and Replace) for the aircraft replacement/ overhaul options, depending on the O&M cost reduction factor (ρ) and the annual lease cost. The boundaries between the three regions are determined by varying the cost reduction factor and calculating the corresponding annual lease cost for a large number of simulation runs (e.g., 100,000). The analysis indicates that there is a critical value of the O&M cost reduction factor (corresponding to the intersection of the three region boundaries) as shown in Figure 2. Decision makers need to estimate the value of the O&M cost reduction factor and compare it with the critical value in order to determine the cost effective option for the CH149 replacement/ overhaul problem. In this example, the Lease region represents the cost effective option where the O&M cost reduction factor is less than 62% to 79% and the lease cost is less than a threshold lease cost of $280M. Similarly, the Replace region indicates the cost effective option when the O&M cost reduction factor is less than the 62% but the lease cost is greater than $280M. Finally, the Upgrade region represents the cost effective option when the O&M cost reduction factor is significantly high.

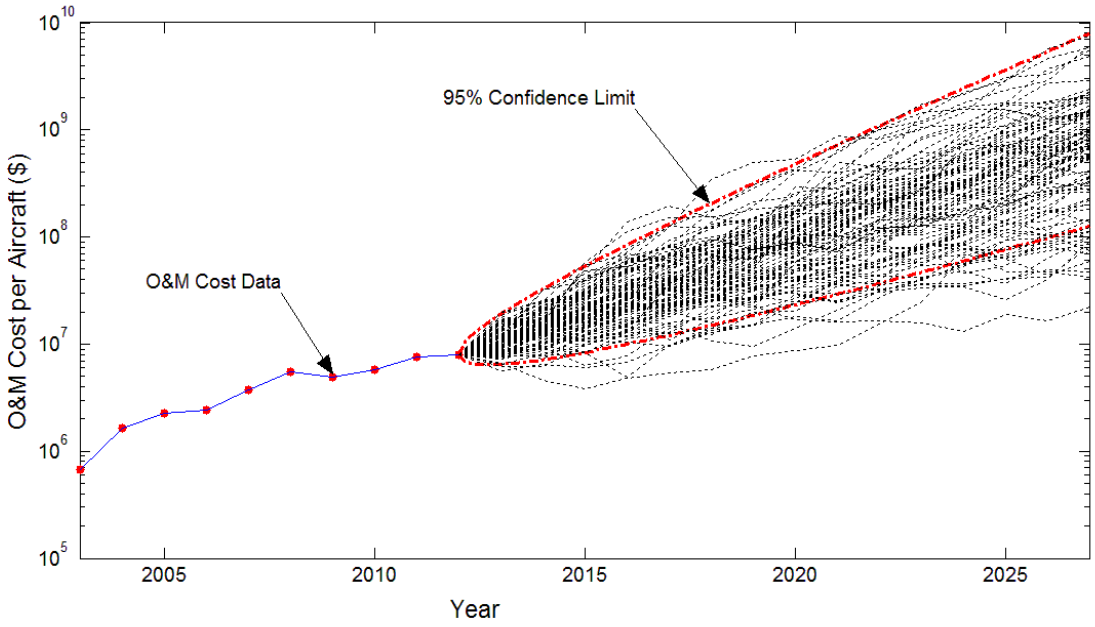

Figure 1. *Aircraft O&M cost data and projected sample paths.*

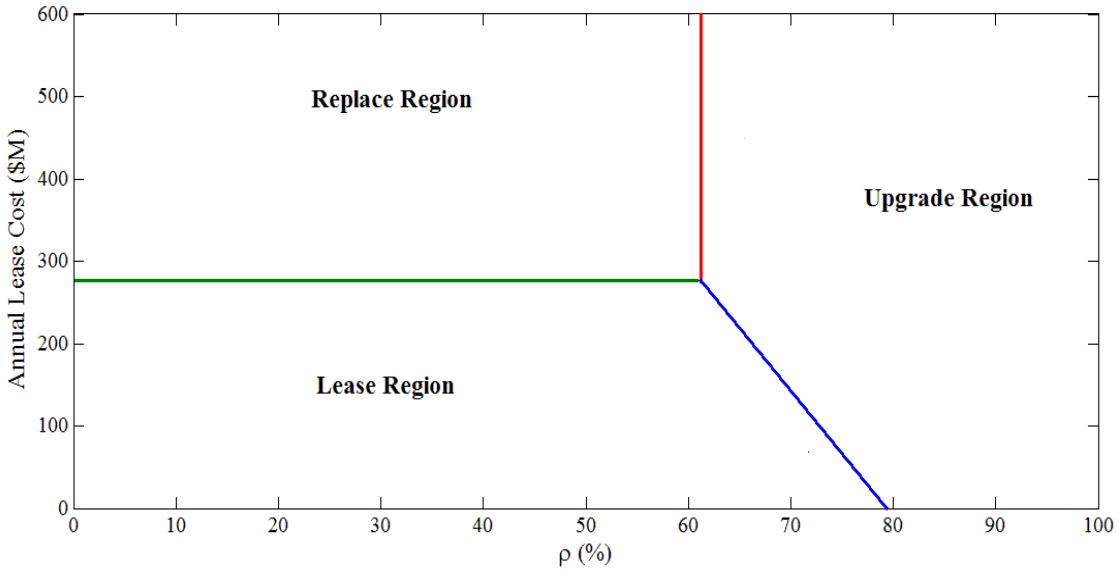

Figure 2. *Decision regions for the aircraft replacement/overhaul options.*

4. Risk and Sensitivity Analysis

An analysis was conducted to evaluate the confidence level for selecting the cost effective option for a given O&M cost reduction factor and a lease cost. The confidence level is determined by calculating the ranking probabilities of the options. Figure 3 depicts the iso-contours of the maximum ranking probabilities of the options and shows different confidence levels for the cost effective regions. The area between the cost effective regions represents the uncertainty region, where all options have comparable ranking probabilities. A sensitivity analysis was also conducted to assess the impact of key parameters (fleet size, in-service period, and O&M cost growth rate) on the cost effectiveness option. It indicates that the decision region would not be affected by a small change in the fleet size but will be sensitive to the in-service period and the O&M cost growth rate.

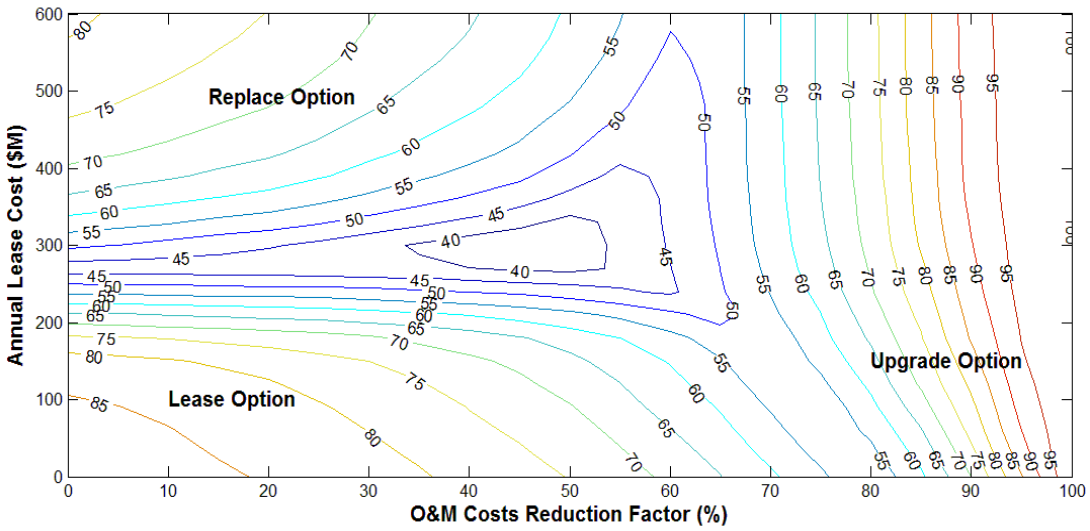

Figure 3. *Iso-Contours of the maximum ranking probabilities.*

5. Conclusions

In this paper, an analysis was conducted to assess the CH149 aircraft replacement/ overhaul options. Depending on the O&M cost reduction factor and the lease cost, three potential decision regions were identified. The analysis indicated that the Upgrade option would not be cost effective as it would not be feasible in practice to reduce the O&M costs by 80%, for example. As such, the Lease or the Replace options should be further investigated. The analysis also indicated that the decision region would not be affected by a small change in the fleet size but will be sensitive to the in-service period and the O&M cost growth rate. Future work would include an analysis of the optimal replacement age of the aircraft.

References

[1] Ghanmi A., G.vanBavel "An Economic Model for Analysing Aircraft Replacement/Overhaul Decisions – Applied to the CH149 Cormorant Mid-Life Upgrade" Defence R&D Canada, Centre for Operational Research and Analysis. DRDC-RDDC-2015-R136 (2015).

[2] Box G.E.P., G.M.Jenkins, G.C.Reinsel "Time Series Analysis: Forecasting and Control" John Wiley &Sons (2008).

[3] Jelon F.C., J.H.Black "Cost and Optimization Engineering" McGraw-Hill, Inc. (1983).

[4] Zylstra R.R. "Normality Tests for Small Sample Sizes" Quality Engineering (1994).

International Journal of Computational and Experimental Science and Engineering (IJCESEN)
Vol. 1-No.2 (2015) pp. 16-19
http://dergipark.ulakbim.gov.tr/ijcesen

ISSN: **2149-9144**

Research Article

Weight Optimization and Reliability Prediction of an Automobile Torque Arm Subjected to Cyclic Loading

Nahide TÜTEN[1]*, Erdem ACAR[1]

[1] *TOBB University of Economics and Technology, Mechanical Engineering Department, Ankara-TURKEY*

* Corresponding Author : ntuten@etu.edu.tr

Presented in "2nd International Conference on Computational and Experimental Science and Engineering (ICCESEN-2015)"

ABSTRACT

The demands for lightweight, high-performance, low-cost structures are dramatically increasing, and that draws attention to research in the field of structural optimization. Designs of lightweight structures have become more important, especially in the automobile industry. The goal of this study is to obtain the optimum shape of an automobile torque arm and predict its reliability. Torque arm, part of the rear suspension, is subjected to cyclic loading. The stresses developed in the structure should not exceed the allowable stress, and fatigue life is another constraint due to cyclic loading. The optimization of torque arm requires calculation of the stresses and the fatigue life many times; therefore surrogate models (response surface approximations and Kriging) are used in this study to reduce the computational cost. Surrogate based optimization of the torque arm is performed by using the Optimization Module of ANSYS Workbench. After the optimum shape is determined, the reliability prediction of the torque arm is performed. In reliability prediction, tail modeling method, an adaptation of a powerful result from extreme value theory in statistics related to the distribution of exceedances, is utilized.

KEYWORDS – Weight Optimization, Surrogate Models, Tail Modeling.

1. Introduction

The limit-state function of a mechanical system is usually evaluated through performing computationally expensive finite element analyses. The simulation techniques such as Monte Carlo method or its advanced variants (e.g., importance sampling, Melchers [1]; adaptive importance sampling, Wu [2]; directional simulation, Nie and Ellingwood [3]) require a large number of limit-state evaluations; hence they are not suitable for highly safe mechanical systems. Alternatively, the analytical methods such as first-/second- order reliability methods (FORM/SORM) are computationally efficient, but their accuracy diminishes as the limit-state function becomes nonlinear. In order to overcome the drawbacks of these traditional methods, the techniques based on tail modeling have been successfully used by many researchers, including Castillo [4], Caers and Maes [5] Kim et al. [6], and Ramu et al. [7] for reliability assessment of highly safe mechanical systems.The demands for lightweight, high-performance, low-cost structures are dramatically increasing, and that draws attention to research in the field of structural optimization. Designs of lightweight structures have become more important especially in automobile industry. The torque arm is a suspension component that mounts on a rear-wheel drive vehicle's rear-drive axle. This component allows the vehicle to accelerate in a straight line without rotating the rear axle. The torque arm also assists the vehicle in braking by applying force to the braking system. The torque arm is primarily used in what designers call a three-link suspension system. In this study, the optimum shape of an automobile torque arm is obtained by using optimization techniques and then the reliability of the optimum configuration is predicted by using tail modeling. The torque arm is subjected to cyclic loading, and it is

designed such that the stresses developed in the structure should not exceed the allowable stress, and fatigue life is another constraint due to cyclic loading. The optimization of torque arm requires calculation of the stresses and the fatigue life many times; therefore surrogate models are used in this study to reduce the computational cost.

2. Problem Definition

In this study, the weight of the torque arm is minimized under stress and life constraints and then its reliability is predicted. The baseline geometry and loading conditions are shown in Figure 1. The torque arm is fixed at the left end to the chassis and the cyclic loads transferred from rear-wheels are applied at the right end. For the loads, a factor of safety of 2.0 is used. For instance, the expected vertical load on the torque arm is 633.25 N, so 1266.5 N vertical load is used in the analysis.

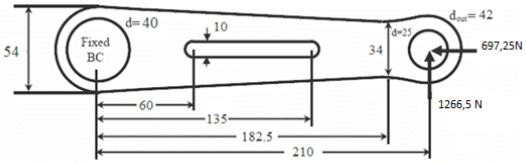

Figure 1. Baseline Geometry and Boundary Conditions Dimensions are in mm.

Based on static and fatigue failure considerations, the optimization formulation can be stated as presented in Eq. (1) and the design variables are shown in Figure 2.

Find d_1, d_2, d_3, d_4, d_5

Minimize $mass\ (d_1, d_2, d_3, d_4, d_5)$

S.t. $Max\ Von\text{-}Mises\ Stress\ (d_1, d_2, d_3, d_4, d_5) - \sigma_{bl} \leq 0$ (1)

$Fatigue\ lifetime\ nf\ (d1, d2, d3, d4, d5) - (nf)bl \leq 0$

where σ_{bl} and $(n_f)_{bl}$ are the maximum von-Mises stress and the fatigue life of the baseline design, respectively. These values are obtained through structural analysis by using ANSYS Workbench Structural Analysis Tool. For fatigue analysis stress-life method [8] is used. The optimization of this problem is performed by using Response Surface Optimization module of ANSYS Workbench. Polynomial response surface (PRS) approximation and Kriging models are used. After the optimum shape is determined, the reliability prediction of the torque arm is performed using tail modeling.

3. Optimization Results

As noted earlier, PRS and Kriging surrogate models are

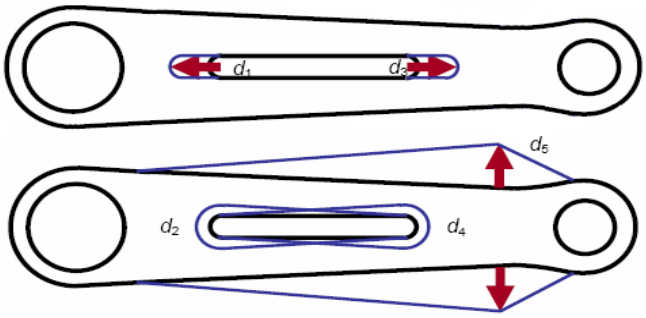

Figure 2. Design variables for the optimization of torque arm

used in this study to relate the maximum von-Mises stress and fatigue life to the design variables. It is found that Kriging surrogate model has smaller RMSE (for both fatigue life and maximum von-Mises stresses) than PRS model, therefore optimization is performed by using Kriging models. Von-Mises stress distribution at the baseline design and the optimum design can be seen in Fig. 3. The values of the design variables, maximum von-Misses stress, fatigue life, and weight of the baseline and the optimum design are given in Table 1. Optimization results indicated that the weight of the torque arm can be reduced by 26% through optimization.

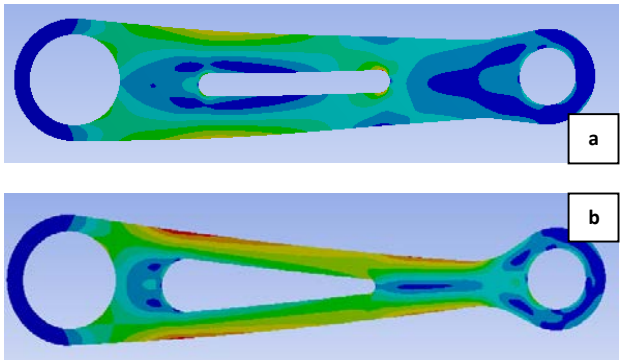

Figure 3. von-Mises stress distribution at (a) the baseline design, (b) the optimum design

4. Reliability Prediction

After obtaining the optimum design, reliability prediction is performed. Random variables are listed in Table 2. The mean values of the geometric random variables are taken as the optimum design dimensions and standard deviation is taken as 1 mm for all geometry random variables. For fatigue life estimation, stress life parameters are strength coefficient (σ_f) and strength exponent (b), and they are taken as random variables. Coefficients of variation values for these parameters are selected based on our experience. Coefficient of variation for load is taken as 0.1 as in [9].

Table 1. Optimization Results

	Baseline Design	**Optimum Design**
Dimensions (mm.)		
d1	60	51
d2	5	11
d3	135	129
d4	5	3
d5	10	18,5
Mass (kg)	0,196	0,145
Max. Von Mises Stress (MPa)	319,6	295,7
Fatigue Life (cycle)	8658	11122

Table 2. Random Variables

Random Variables	**Distribution Type**	**Mean**	**Standard Deviation**
Geometry variables			
d1 (mm)	Normal	51	1
d2 (mm)	Normal	11	1
d3 (mm)	Normal	129	1
d4 (mm)	Normal	3	1
d5 (mm)	Normal	18.5	1
Load Components			
Random Variables	**Dist. Type**	**Mean**	**Standard Deviation**
Fx (N)	Normal	348.625	34.8625
Fy (N)	Normal	633.25	63.325
Fatigue Life Parameters			
Random Variables	**Dist. Type**	**Mean**	**Standard Deviation**
σ_f (MPa)	Lognormal	1043	83.44(Cv=0.08)
b	Normal	-0.107	0.0107(Cv=0.10)

4.1 Reliability Prediction

In this study, tail modeling is used for reliability prediction of the torque arm. Tail modeling method is an adaptation of a powerful result from extreme value theory in statistics related to the distribution of exceedances. The conditional excess distribution above a certain threshold is determined using the *generalized Pareto distribution* (GPD). The distribution parameters of the GPD are found through maximum likelihood estimation [10]. After the distribution parameters are found, the reliability is calculated by using Eq. (2)

$$P_f = 1 - \left(1 - F(g)\right)\left(1 - \frac{\xi}{\sigma} g\right)^{\frac{-1}{\xi}} \quad (2)$$

where ξ is the shape parameter, σ is the scale parameter of GPD, and g is the selected threshold value. For reliability prediction M=500 samples are created according to distribution types, mean and standard deviation values and structural analyses for these samples are performed to obtain fatigue life values. Since the torque arm fails because of fatigue, limit state function is written in terms of fatigue lifetime. The limit state function has the form of

$$g = log(N_c) - \log(N) \quad (3)$$

where system fails g>0 condition, N_c is the critic life determined by finite element analysis of optimum design, and N is the random fatigue life values. Reliability predictions are listed in Table 3. In tail modeling prediction, parameters are calculated using maximum likelihood and least square estimation. The average values of these two methods are also shown.

Table 3. Reliability Prediction

Methods	**Reliability**
Maximum Likelihood Estimation	0.997
Least Square Estimation	0.993
Average	**0.995**

5. Conclusion

This study is mainly concerned with minimization of the weight of an automobile torque arm under stress and fatigue life constraints as well as the reliability prediction of the optimum design. Surrogate based optimization

approach is followed to obtain the optimum torque arm configuration. Polynomial response surface approximations and Kriging metamodels are used, and it is found that Kriging metamodels are more accurate than polynomial response surface approximations. Therefore, Kriging model is further used in used in optimization, which is performed by using Optimization Module of ANSYS Workbench. Optimization results indicated that the weight of the torque arm can be reduced by 26% through optimization. Furthermore, optimum design has better features in terms of maximum von Mises stress and fatigue life. After the optimum design is found, its reliability is predicted by tail modeling technique.

Acknowledgement

The authors gratefully acknowledge the support provided by The Scientific and Technological Research Council of Turkey (TÜBİTAK), under award MAG-214M205.

References

[1] Melchers, R.E., 1989, "Importance Sampling in Structural Systems," Structural Safety, Vol. 6, pp. 3-10. *DOI: 10.1016/0167-4730(89)90003-9*

[2] Wu, Y.T., Shin, Y., Sues, R., and Cesare, M., 2001, "Safety-Factor Based Approach for Probability-Based Design Optimization," Proceedings of the 42rd AIAA/ASME/ASCE/AHS/ASC Structures, Structural Dynamics, and Materials Conference, Paper No. AIAA-2001-1522, Seattle, WA, April 16–19. *DOI: 10.2514/6.2001-1522*

[3] Nie, J., and Ellingwood, B.R., 2000, "Directional Methods for Structural Reliability Analysis," Structural Safety, Vol. 22, pp. 233-249. *DOI:10.1016/S0167-4730(00)00014-X*

[4] Castillo, E., 1988, "Extreme Value Theory in Engineering," Academic Press, San Diego, CA.

[5] Caers, J., and Maes, M., 1998, "Identifying Tails, Bounds, and End-Points of Random Variables," Structural Safety, Vol. 20, pp. 1-23. *DOI:10.1016/S0167-4730(97)00036-2*

[6] Kim, N.H., Ramu, P., and Queipo, N.V., 2006, "Tail Modeling in Reliability-Based Design Optimization for Highly Safe Structural Systems," 47th AIAA/ASME/ASCE/AHS/ASC Structures, Structural Dynamics, and Materials Conference, Newport, RI, AIAA 2006-1825. *DOI: 10.2514/6.2006-1825*

[7] Ramu, P., Kim, N.H., Haftka, R.T., and Queipo, N.V., 2006, "System Reliability Analysis and Optimization Using Tail Modeling," 11th AIAA/ISSMO Multidisciplinary Analysis and Optimization Conference, Portsmouth, VA, AIAA-2006-7012.

[8] Y.-L. Lee, Jwo Pan, Fatigue Testing and Analysis Theory and Practice, Elsevier Inc.,Oxford,2005.

[9] Picheny, V., Kim, N.H., Haftka, R.T., and Quiepo, N.V., 2008, "Conservative Predictions Using Surrogate Modeling," 49th AIAA/ASME/ASCE/AHS/ASC Structures, Structural Dynamics, and Materials, April, Schaumburg, IL. *DOI: 10.2514/6.2008-1716*

[10] E. Acar, Guided tail modeling for efficient and accurate reliability estimation of highly safe mechanical systems, Proceedings of the Institution of Mechanical Engineers Part C: Journal of Mechanical Engineering Science, Vol. 225, No. 5, 1237-1251, 2011. *DOI:10.1177/2041298310392833*

International Journal of Computational and Experimental Science and Engineering (IJCESEN)
Vol. 1-No.2 (2015) pp. 20-23
http://dergipark.ulakbim.gov.tr/ijcesen

ISSN: **2149-9144**

Research Article

An Optimization of Lambda Type assignments via Resource Control[#]

Jelena IVETIĆ[1]*, Silvia GHILEZAN[1], Nenad SAVIĆ[1]

[1]University of Novi Sad, Faculty of Technical Sciences, Novi Sad - Serbia

* Corresponding Author : jelenaivetic@uns.ac.rs

[#] Presented in "2nd International Conference on Computational and Experimental Science and Engineering (ICCESEN-2015)"

Keywords
Lambda calculus
Type assignment
Resource control
Optimization

Abstract: The size of a lambda term's type assignment is traditionally interpreted as the number of involved typing rules, but can be also assessed using some finer-grained measures such as the number of involved type declarations (TD). We propose a type assignment method that relies on the translation of a typeable lambda term to the corresponding term of a modified resource control lambda calculus. The translation output of a given lambda term is often syntactically more complex, therefore more rules need to be used for its type assignment in the target calculus. However, we show that TD measure decreases when types are assigned to terms satisfying a certain minimal level of complexity, thus our method represents an optimization of the lambda calculus' type assignment.

1. Introduction

The untyped λ-calculus is a simple formal system for expressing all effectively computable functions (equivalent to Turing machine). Typed λ-calculus [1] is a restricted system, where application is controlled by objects (types) assigned to λ-terms. Typed λ-calculus has played an important role in the development of programming languages, proof theory, evaluation strategies, mathematical linguistics, etc... Today, a variety of λ-based calculi and type systems have found application in programming languages for certified compilers, automated theorem provers and proof assistants, software verification, etc...

In the λ-calculus, complexity of computation refers to the number of required reduction rules in order to reach the normal form (if possible). For example, in [4], a particular subclass of λ-terms that reduce to normal form in polynomial time is characterized by means of typeability in a system corresponding to light affine logic. Complexity of type assignment, on the other hand, measures the size of type assignment (TA). It can be assessed via different measures, such as: the number of applied TA rules (length of the proof) - time complexity; the number of used type declarations (weight of the proof) - space complexity; the number of used type variables (also weight of the proof, but not interesting for simple types where the type of a given term is unique). The problem of the weight of the proof reducing is interesting for applicative purposes, since it corresponds to the required memory for the type assignment or type checking. The goal of this paper is to investigate the optimization of the lambda type assignment by using the lambda calculus with resource control, $\lambda_{\circledR}$, proposed in [2].

1 RESOURCE CONTROL IN TYPE ASSIGNMENT OPTIMIZATION

The $\lambda_{\circledR}$-calculus is an extension of the λ-calculus with operators that perform quantitative control of variables by explicitly denoting duplication and erasure of each variable, which on the logical side corresponds to structural rules of weakening and

contraction. The *weakening* operator denotes that the variable x does not appear in the term M, whereas the *contraction* operator denotes that two variables x and y play the same role in M, therefore one may think of them as of one duplicated variable z. A detailed account on the $\lambda_{\circledR}$-calculus can be found in [3].

Each λ-term can be represented in the $\lambda_{\circledR}$-calculus using a mapping $[\ ]_{rc}$. In general, a correspondence between sets of λ-terms and $\lambda_{\circledR}$-terms is "one-to-many". It can be showed that the mapping $[\ ]_{rc}$ is constructed in a way that resource operators are put in positions which are optimal from the TA point of view and their interaction is disabled:

Proposition 1. *For each λ-term M, the corresponding $\lambda_{\circledR}$-term $[M]_{rc}$ is in the γω-normal form.*

Simple types are assigned to $\lambda_{\circledR}$-terms by the TA system $\lambda_{\circledR} \rightarrow$. Its main differences with respect to the system $\lambda \rightarrow$ (of simply-typed λ-calculus) are the following: *(i)* two new TA-rules; *(ii)* minimal form of axiom; *(iii)* context-splitting style for the rule with two premises (where Γ,Δ is disjoint union of two bases Γ and Δ). Systems $\lambda \rightarrow$ and $\lambda_{\circledR} \rightarrow$ are represented in Figure 1.

λ →:

$$\frac{}{\Gamma, x : \alpha \vdash x : \alpha}\ (Ax)$$

$$\frac{\Gamma, x : \alpha \vdash M : \beta}{\Gamma \vdash \lambda x.M : \alpha \rightarrow \beta}\ (\rightarrow_{intro})$$

$$\frac{\Gamma \vdash M : \alpha \rightarrow \beta \qquad \Gamma \vdash N : \alpha}{\Gamma \vdash MN : \beta}\ (\rightarrow_{elim})$$

$\lambda_{\circledR}$ →:

$$\frac{}{x : \alpha \vdash x : \alpha}\ (Ax) \qquad \frac{\Gamma, x : \alpha \vdash M : \beta}{\Gamma \vdash \lambda x.M : \alpha \rightarrow \beta}\ (\rightarrow_I)$$

$$\frac{\Gamma \vdash M : \alpha \rightarrow \beta \quad \Delta \vdash N : \alpha}{\Gamma, \Delta \vdash MN : \beta}\ (\rightarrow_E)$$

$$\frac{\Gamma, x : \alpha, y : \alpha \vdash M : \beta}{\Gamma, z : \alpha \vdash z <^{x}_{y} M : \beta}\ (Cont)$$

$$\frac{\Gamma \vdash M : \alpha}{\Gamma, x : \beta \vdash x \odot M : \alpha}\ (Weak)$$

Figure 1. *Type assignment rules for simply typed λ-calculus and for $\lambda_{\circledR}$-calculus*

It is easy to prove the preservation of the type of a λ-term in the system with resource control:

Proposition 2. *If $\Gamma \vdash M : \alpha$ in $\lambda\rightarrow$, then $\Gamma' \vdash [M]_{rc} : \alpha$ in $\lambda_{\circledR} \rightarrow$, for some $\Gamma' \subseteq \Gamma$.*

Our work plan is as follows. For a given λ-term M:

(i) we translate it to corresponding $\lambda_{\circledR}$-term $[M]_{rc}$;

(ii) proposition 2 ensures the preservation of type;

(iii) due to Proposition 1, we can separately investigate the effects of explicit weakening and contraction on the complexity of TA.

Obviously, the number of TA rules will increase because the system $\lambda_{\circledR} \rightarrow$ consists of more rules which reflects the more complex syntax of the $\lambda_{\circledR}$-term, but what about the number of type declarations?

The effect of explicit weakening is firstly investigated on a simple example of a term with *n* void lambda abstractions ($M \equiv \lambda x_n x_{n-1} \ldots x_1.y$) whose counterpart in the $\lambda_{\circledR}$-calculus contains *n* weakenings ($[M]_{rc} \equiv \lambda x_n.x_n \odot (\lambda x_{n-1}.x_{n-1} \odot (\ldots(\lambda x_1.x_1 \odot y)\ldots))$). The type $\alpha_n \rightarrow \alpha_{n-1} \rightarrow \cdots \rightarrow \alpha_1 \rightarrow \beta$ can be assigned to both M and $[M]_{rc}$, but the complexity of TA differs. In the system $\lambda\rightarrow$, the number of applied TA rules is $n + 1$ and the number of used TD is $(n + 1)(n + 2)/2$. On the other hand, in the system $\lambda_{\circledR} \rightarrow$, the number of applied TA rules is $2n + 1$ but the number of used TD is $3n + 1$. Therefore, despite of the increased number of applied TA rules, the total number of used TD is smaller in the presence of explicit weakening for all terms with $n > 3$.

Even in the more general case where *n* void abstractions (i.e. weakenings) are distributed along the term, we obtain that in the system $\lambda \rightarrow$ the number of TD behaves as $O(n^2)$, whereas in the system $\lambda_{\circledR} \rightarrow$ number of TD behaves as $O(n)$.

Next, in order to explore the effect of explicit contraction, we firstly analyze an example of the λ-term with *n* repetitions of the same variable. This is Church numeral representing the natural number N: $N \equiv \lambda f.\lambda x.f^n(x)$. The type int: $(\alpha \rightarrow \alpha) \rightarrow \alpha \rightarrow \alpha$ can be assigned to both N and its resource sensitive counterpart $[N]_{rc}$ which contains *n-1* contractions. In the system $\lambda \rightarrow$, the number of applied TA rules is $2n + 3$; the number of TD: $4n + 3$. In the system $\lambda_{\circledR} \rightarrow$, the number of TA rules is $3n + 2$; the number of TD: $6n - 1$. In both cases the number of TD behaves as $O(n)$, but without explicit contraction it is smaller for $n \geq 2$. Therefore, in spite of the presence of the context splitting rule for application which decreases number of TD, explicit contraction in general does not contribute to the optimization of the type assignment complexity. An explanation for

this phenomenon lies in the fact that apart from the additional TA rules, the number of TD is enlarged because all fresh variables need to be declared. This neutralizes the positive effect of the context-splitting rule.

Conclusion of analysis of effects: In case of the explicit weakening, it is not possible to separate two additional features of the system $\lambda_{\circledR} \rightarrow$: the minimal axiom and the new rule *(Weak)*. But, in case of the explicit contraction, it is possible to separate two additional features of the system: context splitting form of the rule *(→E)* and the new rule *(Cont)*. Thus, we can build a novel, *hybrid system* $\lambda^o\rightarrow$, collecting only those features that reduce the number of TD:

(i) explicit weakening;
(ii) implicit contraction;
(iii) partial context-splitting form of the rule *(→E)* (with ordinary union $\Gamma \cup \Delta$ instead of disjoint one Γ,Δ).

Syntax

Pre-terms:

$$M, N \quad ::= \quad x \mid \lambda x.M \mid MN \mid x \odot M$$

Terms are pre-terms that satisfy the condition:

in

$$\lambda x.M \quad x \in Fv(M)$$

Reductions

$$\begin{array}{lrcl} (\beta) & (\lambda x.M)N & \rightarrow & M[N/x] \\ (\omega_1) & \lambda x.(y \odot M) & \rightarrow & y \odot (\lambda x.M) \\ (\omega_2) & (x \odot M)N & \rightarrow & x \odot (MN) \\ (\omega_3) & M(x \odot N) & \rightarrow & x \odot (MN) \end{array}$$

Mapping from λ

$$\begin{array}{rcl} [x]_o & = & x \\ [MN]_o & = & [M]_o[N]_o \\ [\lambda x.M]_o & = & \begin{cases} \lambda x.[M]_o, & x \in Fv(M) \\ \lambda x.x \odot [M]_o, & x \notin Fv(M) \end{cases} \end{array}$$

System λ^o→

$$\frac{}{x : \alpha \vdash x : \alpha}\ (Ax)$$

$$\frac{\Gamma, x : \alpha \vdash M : \beta}{\Gamma \vdash \lambda x.M : \alpha \rightarrow \beta}\ (\rightarrow_I)$$

$$\frac{\Gamma \vdash M : \alpha \rightarrow \beta \quad \Delta \vdash N : \alpha}{\Gamma \cup \Delta \vdash MN : \beta}\ (\rightarrow_E)$$

$$\frac{\Gamma \vdash M : \alpha}{\Gamma, x : \beta \vdash x \odot M : \alpha}\ (Weak)$$

***Figure** 2. The λ^o – calculus*

The syntax and reduction rules of the λ^o-calculus, the mapping $[\ ]_o$ from λ to λ^o , and type assignment system $\lambda^o\rightarrow$ are given in Figure 2.

Turning back to Church numeral N and the type assignment of its corresponding term $[N]^o$ in the system $\lambda^o\rightarrow$, we obtain the following results: the number of TA rules is $2n + 3$; the number of TD: $3n + 2$ (which is less than in $\lambda\rightarrow$ for all n). Finally, some additional results for several randomly chosen terms, typed in parallel in the systems $\lambda\rightarrow$ and $\lambda^o\rightarrow$ are given in Table 1. Since some terms are too long to fit in the table, we will give their standard interpretation instead of the syntax. For example, we will write 3 for $\lambda f.\lambda x.f(f(fx))$, MULT for $\lambda x.\lambda y.\lambda z.x(yz)$, FALSE for $\lambda x.\lambda y.y$, etc… We will also use prefix notation for binary operations. For example, PLUS 10 (MULT 5 2) stands for $10 + 5*2$.

***Table** 1. Some empirical results*

(meaning of) the term	Number of TD in $\lambda\rightarrow$	Number of TD in $\lambda^o\rightarrow$	% of improvement
MULT 3 2	44	30	32%
PLUS 10 (MULT 5 2)	137	90	34%
AND TRUE FALSE	17	14	18%
λw.(λx.yz)(uv)	47	26	45%

2 CONCLUSION

The λ^o-calculus is a modified version of the $\lambda_{\circledR}$-calculus, which preserves good properties of the system $\lambda_{\circledR} \rightarrow$ relevant for the optimization issues. Except for the limited number of simple terms, it reduces the type assignment procedure in terms of the number of type declarations, thus optimizing required space (= memory) for type checking, which makes it suitable for applications. To review the full extent of the proposed optimization method, we will in the future conduct semi-automated testing with large-scale terms. Also, it would be interesting to extend the proposed method to more complex type-systems (such as intersection types, polymorphic types, dependent types,...) and to other lambda-based formal calculi.

REFERENCES

[1] H. P. Barendregt, W. Dekkers, and R. Statman. Lambda Calculus with Types. Perspectives in logic. Cambridge University Press, 2013.

[2] S. Ghilezan, J. Ivetić, P. Lescanne, and S. Likavec. Intersection types for the resource control lambda calculi. In A. Cerone and P. Pihlajasaari, editors, 8th International Colloquium on Theoretical Aspects of Computing, ICTAC '11, volume 6916 of Lecture Notes in Computer Science, pages 116–134. Springer, 2011. *DOI: 10.1007/978-3-642-23283-1_10*

[3] S. Ghilezan, J. Ivetić, P. Lescanne, and S. Likavec. Resource control and intersection types: an intrinsic connection. CoRR, abs/1412.2219, 2014.

[4] P. Baillot, K. Terui. Light types for polynomial time computation in lambda calculus. Information and Computation, volume 207, pages 41-62. Elsevier, 2009. *DOI:10.1016/j.ic.2008.08.005*

International Journal of Computational and Experimental Science and Engineering (IJCESEN)
Vol. 1-No.2 (2015) pp. 24-26
http://dergipark.ulakbim.gov.tr/ijcesen

ISSN: **2149-9144**

Research Article

A New Approach for Solving Linear Fredholm Integro-Differential Equations#

Gül Gözde BİÇER[1], Yalçın ÖZTÜRK[2], Mustafa GÜLSU[1]

[1]Department of Mathematics, Faculty of Science, Mugla Sitki Kocman University, Mugla, Turkey
[2]Ula Ali Kocman Vocational School, Mugla Sitki Kocman University, Mugla, Turkey

* Corresponding Author : gulgozdebicer@hotmail.com

Presented in "2nd International Conference on Computational and Experimental Science and Engineering (ICCESEN-2015)"

Keywords
Fredholm
integro-differantial equation
Bernoulli polynomials
Numerical solutions

Abstract: In this paper a numerical method is given for the solution of linear Fredholm integro differential equations under the mixed conditions using the Bernoulli polynomials. Finally, some experiments and their numerical solutions are given. The results reveal that this method is very effective and highly promising when compared with other numerical methods.

1 Introduction

Many physical problems are modelled by integral or integro differential equations. Historically, they have achieved great popularity among mathematicians and physicists in formulating boundary value problems of gravitation, electrostatics, fluid dynamics and scattering. It is also well known that initial-value and boundary-value problems for differential equations can often be converted into integral equations and there are usually significant advantages to be gained from making use of this conversion. Among these equations, Fredholm integro-differential equations (FIDEs) arise from various applications, like engineering, biology, medicine, economics, potential theory and many others.

The technique that we used is a numerical solution method, which is based on numerical solution of linear differential equations with variable coefficients in terms of Bernoulli polynomials.

In this study, the basic ideas of the above studies are developed and applied to the m^{th}-order linear Fredholm integro differential equation with variable coefficients

$$\sum_{k=0}^{m} P_k(x)y^{(k)}(x) = g(x) + \lambda_1 \int_a^b K_f(x,t)y(t)dt \quad (1)$$

for $0 < a \le x,t \le b < \infty$

under the mixed conditions,

$$\sum_{k=0}^{m-1}\left[a_{ik}y^{(k)}(a) + b_{ik}y^{(k)}(b)\right] = \mu_i \quad (2)$$

for $i = 0,1,2,\ldots,m-1$.

and the solution is expressed in the form,

$y(x) = \sum_{n=0}^{N} a_n B_n(x)$ which is a Bernoulli polynomial of degree N and a_n are unknown Bernoulli coefficients.

2 Fundamental Matrix Solution

Let us consider the m th-order Fredholm integro differential equation with variable coefficients (1) and find the matrix forms of each term of equation.

$\sum_{k=0}^{m} P_k(x)y^{(k)}(x) = g(x) + \lambda_1 \int_a^b K_f(x,t)y(t)dt$, or shortly $\sum_{k=0}^{m} P_k(x)y^{(k)}(x) = g(x) + \lambda_1 I_f(x)$ where $I_f(x) = \int_a^b K_f(x,t)y(t)dt$. Then we write the matrix form of $y(x)$ is $y(x) = \mathbf{B}(x)\mathbf{A}$

where $\mathbf{B}(x) = [B_0(x) \quad B_1(x) \quad \cdots \quad B_N(x)]$, $\mathbf{A} = [a_0 \quad a_1 \quad \cdots \quad a_N]^T$. By using the general representation of Bernoulli polynomials which is $B_N(x) = \sum_{i=0}^{N} \binom{N}{i} b_N x^{N-i}$ we can write $y(x)$ for variable t, $y(t) = \mathbf{B}(t)\mathbf{A}$ using the Maclaurin expansion,

$$K_f(x,t) = \mathbf{X}(x)\mathbf{K}_t\mathbf{X}^T(t), \qquad \mathbf{K}_t = [k_{ij}^t], \quad (3)$$

$i, j = 0,1,2,\ldots, N$

and then using the Bernoulli expansion,

$$K_f(x,t) = \mathbf{B}(x)\mathbf{K}_f\mathbf{B}^T(t), \qquad \mathbf{K}_f = [k_{ij}^f], \quad (4)$$

$i, j = 0,1,2,\ldots, N$

we find

$$\mathbf{X}(x)\mathbf{K}_t\mathbf{X}^T(t) = \mathbf{B}(x)\mathbf{K}_f\mathbf{B}^T(t) \Rightarrow$$
$$\mathbf{X}(x)\mathbf{K}_t\mathbf{X}^T(t) = \mathbf{X}(x)\mathbf{S}\mathbf{K}_f\mathbf{S}^{\mathbf{T}}\mathbf{X}^T(t) \Rightarrow$$
$$\mathbf{K}_t = \mathbf{S}\mathbf{K}_f\mathbf{S}^T \Rightarrow \mathbf{K}_f = \mathbf{S}^{-1}\mathbf{K}_t(\mathbf{S}^{\mathbf{T}})^{-1}.$$

On the other hand, $\mathbf{B}(x) = \mathbf{X}(x)\mathbf{S}$ using this relation we can find

$$\mathbf{X}^{(k)}(x) = \mathbf{X}(x)\mathbf{M}^k \quad \Rightarrow y^{(k)}(x) = \mathbf{X}(x)\mathbf{M}^k\mathbf{S}\mathbf{A}.$$

And then we obtain

$$I_f = \int_a^b \mathbf{B}(x)\mathbf{K}_f\mathbf{B}^T(t)\mathbf{A}dt = \mathbf{B}(x)\mathbf{K}_f\mathbf{Q}_f\mathbf{A} \quad (5)$$

where $\mathbf{Q}_f = \int_a^b \mathbf{B}^T(t)\mathbf{B}(t)dt$.

We can write $\mathbf{Q}_f$ also,

$$\mathbf{Q}_f = \int_a^b \mathbf{B}^T(t)\mathbf{B}(t)dt = \int_a^b \mathbf{S}^T\mathbf{X}^T(t)\mathbf{X}(t)\mathbf{S}dt = \mathbf{S}^T\underbrace{\left[\int_a^b \mathbf{X}^T(t)\mathbf{X}(t)dt\right]}_{\mathbf{H}_f}\mathbf{S}$$

$$\mathbf{H}_f = [h_{ij}^f(x)], \qquad h_{ij}^f(x) = \int_a^b \mathbf{X}^T(t)\mathbf{X}(t)dt = \frac{b^{i+j+1} - a^{i+j+1}}{i+j+1}$$

$i, j = 0,1,2,\ldots, N$.

Then we obtain $\mathbf{Q}_f = \mathbf{S}^T\mathbf{H}_f\mathbf{S}$ using this relation we find $\mathbf{I}_f(x) = \mathbf{X}(x)\mathbf{S}\mathbf{K}_f\mathbf{Q}_f\mathbf{A}$. As a result, the matrix representation of

$$\sum_{k=0}^{m} P_k(x)y^{(k)}(x) = g(x) + \lambda_1 \int_a^b K_f(x,t)y(t)dt$$

can be given by $\sum_{k=0}^{m} \mathbf{P}_k y^{(k)} = \mathbf{G} + \lambda_1 \mathbf{I}_f$. On the other hand using the relation $y^{(k)}(x) = \mathbf{X}(x)\mathbf{M}^k\mathbf{S}\mathbf{A}$, the matrix form of the conditions given by (2) can be written as $\sum_{k=0}^{m-1} [a_{ik}\mathbf{X}(a) + b_{ik}\mathbf{X}(b)]\mathbf{M}^k\mathbf{S}\mathbf{A} = \mu_i$

$i = 0,1,2,\ldots, m-1$

3 Method Of Solution

We are ready to construct the fundamental matrix equation corresponding to Eq.(1). For this propose, firstly we write

$\sum_{k=0}^{m} P_k(x)y^{(k)}(x) = g(x) + \lambda_1 I_f(x)$ and then we can write $x = x_i = a + \frac{b-a}{N} i$, $i = 0,1,2,\ldots, N$ and then we obtain $\sum_{k=0}^{m} P_k(x_i)y^{(k)}(x_i) = g(x_i) + \lambda_1 I_f(x_i)$, $i = 0,1,2,\ldots, N$ so the fundamental matrix equation is gained $\sum_{k=0}^{m} \mathbf{P}_k y^{(k)} = \mathbf{G} + \lambda_1 \mathbf{I}_f$. Then, we obtain

$$\sum_{k=0}^{m}\mathbf{P}_k\mathbf{X}\mathbf{M}^k\mathbf{S}\mathbf{A}=\mathbf{G}+\lambda_1\left(\mathbf{X}\mathbf{S}\mathbf{K}_f\mathbf{Q}_f\mathbf{A}\right)\Rightarrow$$

$$\underbrace{\left(\sum_{k=0}^{m}\mathbf{P}_k\mathbf{X}\mathbf{M}^k\mathbf{S}-\lambda_1\mathbf{X}\mathbf{S}\mathbf{K}_f\mathbf{Q}_f\right)}_{\mathbf{W}_f}\mathbf{A}=\mathbf{G} \qquad (6)$$

The fundamental matrix equation (6) for Eq.(1) corresponds to a system of (N+1) algebraic equation for the (N+1) unknown coefficients $a_0, a_1, a_2,..., a_N$. Briefly, we can write (6)

$$\mathbf{W}_f\mathbf{A}=\mathbf{G} \text{ or } \left[\mathbf{W}_f;\mathbf{G}\right] \qquad (7)$$

And briefly, the matrix form for conditions (2) is,

$$\mathbf{U}_i\mathbf{A}=\left[\mu_i\right] \text{ or } \left[\mathbf{U}_i;\mu_i\right],\ i=0,1,2,...,m-1 \qquad (8)$$

To obtain the solution of Eq.(1) under the conditions (2), by replacing the rows matrices (8) by the last m rows of the matrix (7) we have the required augmented matrix or corresponding matrix equation $\mathbf{W}_f{}^*\mathbf{A}=\mathbf{G}^*$. If $rank\left(\mathbf{W}_f{}^*\right)=rank\left[\mathbf{W}_f{}^*;\mathbf{G}^*\right]=N+1$ we can write $\mathbf{A}=\left(\mathbf{W}_f{}^*\right)^{-1}\mathbf{G}^*$ Thus the coefficients a_i, $i=0,1,2,...,N$ are uniquely determined by the last equation.

4 Conclusion

Integro differential equations are usually difficult to solve analytically. In many cases, it is required to obtained the approximate solution. For this propose, the present method can be proposed. In this paper, Bernoulli polynomial approach has been used for the approximate solution of linear Fredholm integro differential equations. The proposed method is suggested as an efficient method for linear Fredholm integro differential equations

References

[1] M. Sezer, M. Gulsu, A new polynomial approach for solving difference and Fredholm integro-differential equation with mixed argument, Appl. Math. Comput. 171 (2005) 332-344.

[2] P. Natalini, A. Bernaridini, A generalization of the Bernoulli polynomials, J. Appl. Math. 3 (2003) 155–163.

[3] E. Tohidi, A.H.Bhrawy, K.Erfani, A collocation method based on Bernoulli operational matrix for numerical solution of generalized pantograph equation, Appl. Math. Model. 37 (2013) 4283-4294.

International Journal of Computational and Experimental Science and Engineering (IJCESEN)
Vol. 1-No.2 (2015) pp. 27-30
http://dergipark.ulakbim.gov.tr/ijcesen

ISSN: **2149-9144**

Research Article

A Computational Method for Analysis of EPR Spectra Based on Image Processing

Mustafa Reşit TAVUS[1*], Yunus ÇELIK[2],Nurettin ŞENYER[1], Recai OKTAŞ[1], and Bünyamin KARABULUT[1]

[1]Ondokuz Mayıs University, Faculty of Engineering, Department of Computer Engineering, 55125, Samsun-Turkey
[2]Ondokuz Mayıs University, Faculty of Arts and Science, Department of Physics, 55125, Samsun-Turkey

* Corresponding Author : mustafa.tavus@bil.omu.edu.tr

Presented in "2nd International Conference on Computational and Experimental Science and Engineering (ICCESEN-2015)"

Keywords
Image processing
Spectrum analysis
Peak detection
EPR
Gamma irradiation

Abstract: In this study, it was aimed to finish the analysis process much quicker and make the error margin minimum. Image processing technique was applied to the spectra of gamma irradiated diammonium hydrogen citrate single crystals recorded in the electron paramagnetic resonance (EPR) spectrometer. The peak values in the analogue spectra were detected and transferred to digital environment by using the image process technique. The analogue structures of the spectra were reobtained by using curve fitting methods after the digital spectra were implemented some basic morphological image processing techniques. The spin-Hamiltonian parameters were calculated by using the spectra acquired in our calculation and a comparison made with the results of manually resolved spectra. In this way, the aim of the study was achieved by minimizing the loss of time spent in the analysis stage and the errors related to humans.

1. Introduction

Human factor plays an important role in the analysis of scientific spectra. It can cause the analysis to last longer and the error margin to increase more during the analysis. Since the mistakes made during the measurements of both scan field and amplitudes in the spectra affect the results of analysis, making the errors minimum and having the same success in all spectra are very important at this stage [1].

There are a lot of studies on the spectra since they are used in many different scientific fields such as physics, chemistry, medicine, and engineering. Some researchers studied about peak detection [2], curve fitting methods [3], and image enhancements [4]. A group of researchers from the field of engineering analyzed the electromyography signal by using spectrogram in 2013. In the study, they investigated the effect of signal analysis on image size [5].

It is very important to obtain the spectra correctly for paramagnetic centers having different hyperfine values and line intensities in EPR spectroscopy. It lasts weeks even months to calculate the hyperfine values and g factors of paramagnetic centers, which has a lot of lines in its EPR spectra. Taking care of distribution of line intensities in typical EPR spectra, the spectra can be converted to digital medium and used image processing techniques to evaluate both g factors and hyperfine values in a very short time.

In this study, our aim was to minimize human errors in the analysis of spectra by using image processing techniques. A software was developed to analyze the spectra and the results were compared with those obtained manually.

2. Material and Method

There are five algorithmic steps in the study and these steps are explained in detail as below.

2.1. Obtaining Spectra

The images used in the study were obtained from the EPR spectra of gamma irradiated diammonium hydrogen citrate single crystals. The spectra were recorded on an EPR spectrometer between 0° and 180° at 10° steps for each three mutually perpendicular axes, i.e. x, y, z axes.

2.2. Preprocessing

After first step, the spectra were transferred to a computer by a scanner. The digitized images had 2480*1753 pixels resolution. The images transferred to computer were cleaned from environmental noises and factors that can cause incorrect results by using Matlab (R) R2012a (7.14.0.739) 32-bit (win32). One of the important parts in the analysis of spectra is to locate the center point. To overcome this problem, the center point was marked. This mark would be used in detection of center points of the other spectra. A spectrum after completing pre-processing step is shown in Figure1.

2.3. Image Processing Techniques

Some image processing techniques were required to analyze the spectra in best way. To make the detection of points in spectra easier and more precise, all images were converted from RGB (red-green-blue) to BW (black-white). A morphological process named the erosion was applied to remove linear noises. After these processes, the spectra were provided to be more linear. Since the spectral images were based on pixels, the points of the spectra were detected by scanning both x and y axes. In BW image, "0" shows background and"1" shows the points of the spectra.

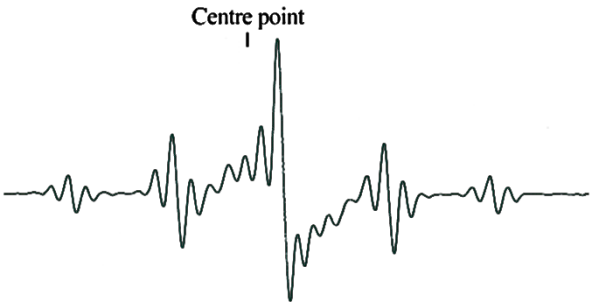

Figure 1. *One of the spectra after preprocessing step.*

2.4. Point Extraction

In the preceding part, the general outline of the spectra was somewhat appeared. To continue resolving the spectra, we need to know the corresponding values of all points. Hence, the points were converted from pixels to gauss (magnetic field unit) as well as intensity and new coordinate values were assigned for each points. The central gauss value in the spectra was taken into account when converting pixels to gauss value. For example, if the magnetic field magnitude is chosen as 3000 gauss when recording the spectra, then the central gauss value is 3000 gauss and the value will increase or decrease due moving to the right or left of the center, respectively.

2.4.1. Curve Fitting

After all these steps, the spectra are still composed of points. Hence, to continue analyzing the spectra, the points have to be combined together by using correct curve fitting method. In this study, we used smoothing spline method, which is a polynomial method. Previous studies showed that smoothing spline method is also successful at image enhancement [6]. We applied different curve fitting methods before using smoothing spline and noticed that the smoothing spline method had a greater successful rate than the other methods. We selected '0.94' as sensitivity value since it gave the best results. The digitized images which are very similar to the original spectra were obtained by using the smoothing spline method.

2.4.2. Peak Detection

The most important part in spectrum analysis is to detect local maximum and minimum points (peaks) because the analysis is based on this situation. The more we choose appropriate points among the peaks in the spectrum, the more the result of analysis will be successful. To detect peaks, we used the method, with some minor changes and improvements, developed in 2012 by Billauer [7].

Two arguments were needed to detect peaks: vector and delta. The vector represents the points that create the spectrum. Delta is the threshold value for a peak. If the difference between two points is greater than delta value, the point having the greater value is detected as peak. Here the important thing is how to detect delta threshold value because the delta threshold value has different values in each spectrum. In the study, we realized that the delta threshold value has a value between 1 and 10 for all spectrum. We used an algorithm shown in Figure 2.a and detected optimal delta value for each spectrum.

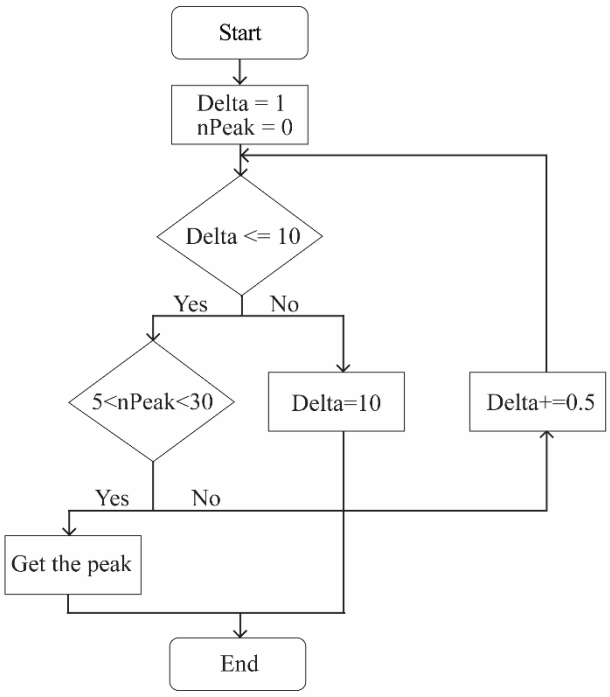

Figure 2.a. *The algorithm of detection delta threshold value.*

We detected all peaks in the spectrum after optimal delta value was found. However, in the analysis, we need only points that show sudden and major changes. To do this, we need to detect points over an identified threshold value. We determined this threshold value as the first detected value of intensity point and we realized that this method is successful for all spectra. Figure 2.b shows one of the spectra after this step.

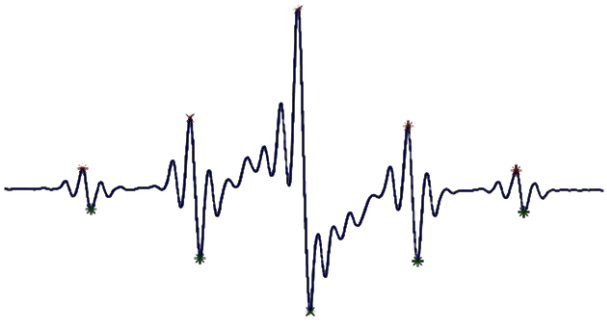

Figure 2.b. *Detected peaks over identified threshold value in one of the spectra.*

Although we detected peaks, we needed fewer points which represented the spectrum better. To select these peaks, we used a method that the points close to each other were collected in a cluster. When the distance of two points is over some specific value, which is related to hyperfine value in EPR, the points were collected in a cluster. Later, the areas under peaks were calculated in the clusters and compared with each other in its own cluster. A peak which has the largest area in its cluster was selected as point used in the analysis stage. This process was applied to all clusters and a single peak was found for each cluster. The determined peaks having the largest area are shown in Figure 2.c.

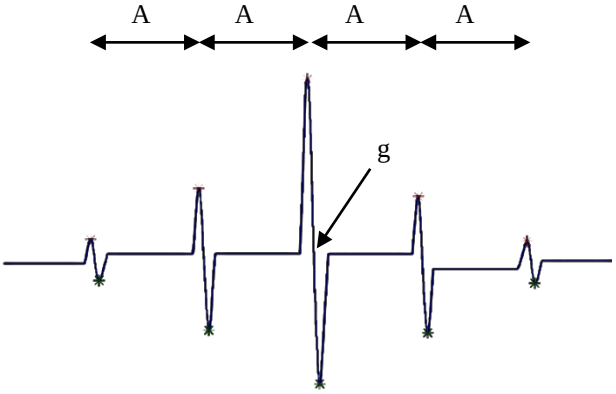

Figure 2.c. *The peak points detected with area*

2.5. Evaluation of obtained points

In the stage of detection of peaks, the peaks were selected to be used in the analysis. To analyze spectrum, the gauss values of points were saved as a text output that used in evaluation application. The signal analysis was completed after all these steps and evaluation of signal was initiated.

3. Results and Discussion

In paramagnetic centres, the interaction between the nucleus and the unpaired electron is called hyperfine interaction and is equal to the spacing between adjacent peaks in units of millitesla (mT) [8]. In EPR spectroscopy the g factor is a measure of the magnetic property of the paramagnetic environment and is also known as spectroscopic splitting factor [8]. These two values, hyperfine and g factor, are visualized in Figure 2.c.

The g factors and hyperfine values for gamma irradiated diammonium hydrogen citrate single crystals are evaluated first manually and then by using the image process algorithm described above. In manual evaluation, the values of each peak in recorded spectra were obtained by using a ruler and then calculations were made. The duration for the whole process is about three weeks. However, the duration for the same process is about a couple of hours by using the method we developed in the study.

To calculate g factors and hyperfine values, one needs to plot a graph g^2 against rotation angle in EPR spectra. Figure 3 shows the graphs plotted for the first plane, i.e. *ab* plane, by using both experimental and computational data. We used the fitting procedure and calculation technique as described in [8, 9]. The calculated g factors and hyperfine values

for both methods are within the experimental error range and as follows: g_{exp}=1.999, A_{exp}=3.11 mT, g_{comp}=1.994, A_{comp}=3.16 mT.

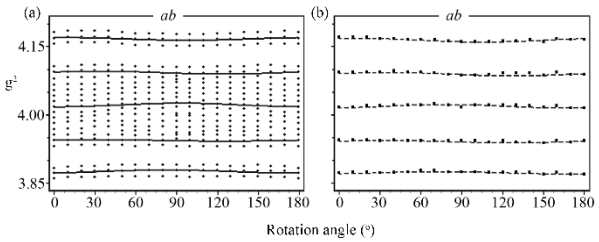

Figure 3. *Plot of g^2 vs rotation angle in ab plane by using (a) experimental and (b) computational data.*

4. Conclusion

Complex EPR spectra can be simplified by removing the noise from the spectrometer. We tried to simulate the EPR spectra recorded for irradiated diammonium hydrogen citrate single crystals. By using the algorithm provided above, the desired simple and ready to use spectra were obtained in a couple of minutes rather than weeks. One can also use the algorithm to distinguish paramagnetic centres with different hyperfine values. The paramagnetic centres can be complexes doped with transition metal ions, irradiated single crystals, or biological radical centres.

References

[1] W. Yiding, W.Yunhong, and Z. Shi, Errors analysis of spectrum inversion methods, Proc. IEEE International Conference on Signal Processing and Communications (ICSPC 2007), 24-27 November, 2007 Dubai-United Arab Emirates

[2] E. Min, M.Ko, Y. Kim, J.Joung, and K. Lee, A peak detection in noisy spectrum using principal component analysis, Proc.IEEE Nuclear Science Symposium and Medical Imaging Conference (2012 NSS/MIC), 27 October - 03 November, 2012 Anaheim, CA-USA

[3] R. Sun, H. Z. Huang, J. Yang, D. Ling, and Q. Miao, Curve fitting with weight assignment under evidence theory combination rule, Proc. 2011 International Conference on Quality, Reliability, Risk, Maintenance, and Safety Engineering (ICQR2MSE), 17-19 June, 2011 Xi'an-China

[4] S.Premkumar and K. A.Parthasarathi, An efficient approach for colour image enhancement using Discrete Shearlet Transform, Proc. 2nd International Conference on Current Trends in Engineering and Technology (ICCTET 2014), 8 July, 2014 Coimbatore-India

[5] T. N. S. T. Zawawi, A. R. Abdullah, E. F. Shair, I.Halim, and O. Rawaida, Electromyography signal analysis using spectrogram, Proc. 2013 IEEE Student Conference on Research and Development (SCOReD 2013), 16-17 December, 2013 Putrajaya-Malaysia

[6] F. Precioso, M. Barlaud, T. Blu, and M. Unser, Robust real-time segmentation of images and videos using a smooth-spline snake-based algorithm, IEEE Transactions on Image Processing 14 (2005) 910-924. DOI: 10.1109/TIP.2005.849307

[7] E. Billauer, http://www.billauer.co.il/peakdet.html, Access date, 28.09.2015

[8] B. Karabulut and R. Tapramaz, EPR study of gamma irradiated arsanilic acid single crystal, Radiation Physics and Chemistry 55 (1999) 331-335. DOI:10.1016/S0969-806X(98)00348-X

[9] R. Biyik, M. Cemberci, and R. Tapramaz, A Computer Program to Help Resolution of Complex and Poorly Resolved Cu^{2+} and VO^{2+} Ions Doped Single Crystals Electron Paramagnetic Resonance Spectra, Spectroscopy Letters 42 (2009) 436-441. DOI:10.1080/00387010903253831

International Journal of Computational and ExperimentalScience and Engineering (IJCESEN)
Vol. 1-No.2 (2015)pp. 31-35
http://dergipark.ulakbim.gov.tr/ijcesen

***ISSN:*2149-9144**

ResearchArticle

Rotation Invariant Features Based on Regional Rank for Texture Classification[#]

Farida OUSLIMANI[1,2]*, Achour OUSLIMANI [2], Zohra AMEUR[1]

[1]LAMPA Laboratory, University of Mouloud Mammeri,Tizi ouzou, Algeria.
[2] QUARTZ Laboratory, Graduate school in electrical engineering (ENSEA), Cergy, France.

* CorrespondingAuthor : ouslimani.f@gmail.com

[#] Presented in "2nd International Conference on Computational and Experimental Science and Engineering (ICCESEN-2015)"

Keywords
Texture descriptor
regional rank
rotation invariance
texture classification

Abstract: In this paper, we present rotation invariant descriptors using regional rank for texture classification. The regional rank presents the rank of the gray level of each pixel in a region whose size and shape depend on the gray level of the treaty pixel and its neighbors. Rotation invariant features are obtained by combining the rank which is found and the treaty pixel code. This latter is calculated by global thresholding. Eight discriminates and rotation invariant features are then obtained. The features size don't increase with scale and kept constant. Tests are performed on the well known Outex database. Compared to LBP method using different schemes, the proposed method achieves good texture classification performance while enjoying a compact feature representation.

1. Introduction

Texture analysis is an active research topic in image processing and pattern recognition. However, arbitrary rotation could occur in real-world textures. It will affect the performance of the texture analysis methods. Thus, extracting texture features that are rotation- invariant is an important issue to be addressed.

Many methods were proposed for rotation invariance [1].Early ones focus on the statistical analysis of texture images. This starts with the co-occurrence matrix method [2].Later, many model-based methods were proposed for rotation invariance, such as circular autoregressive model [3] and markov random fields [4-6]. Rotation invariant features obtained through filter bank responses are also used [7-9]. Recently, Ojala et al. [10] proposed a local binary pattern (LBP) histogram for rotation invariant texture classification. LBP is a simple yet efficient operator to describe local image pattern, and it has achieved impressive classification results on representative texture databases [11].Many extensions of LBP were presented [12-14].

In [15], we introduced regional rank coding method. In order to extract more discriminate texture pattern, some modifications were conducted. First, to acquire more precision,regional rank ratio is portioned in four intervals and not two. Second, the gray level information is used for coding after global thresholding. Thus, eight rotation invariant patterns are obtained. Third, different neighbourhood search space dimension are exploited. Also, the features histogram has the same size in different scales. So, they can be easily fused to improve the texture classification accuracy.

The rest of the paper is organized as follows. Section 2 reviews briefly LBP. Section 3 presents the proposed features. Section 4 reports the experimental results on large public texture database. Finally, Section 5 concludes the correspondence.

2. Brief review of Local binary Pattern (LBP)

LBP is initially proposed by Ojala et al. [16] to support the local contrast measure of image. The spatial structure of a local image texture is characterized by thresholding a 3×3 square neighbourhood with the value of the center pixel. To allow multi-resolution analysis and rotation invariance a more general formulation defined on circular symmetric neighborhood was proposed in [10] .The LBP pattern is computed by comparing the value of the center pixel x_c with those of its P neighbors that are evenly distributed on a circle of radius R centred at center x_c , such that the LBP response is calculated as

$$LBP_{R,P} = \sum_{i=0}^{P-1} s(x_i - x_c)\, 2^i, \quad s(x) = \begin{cases} 1 & x \geq 0 \\ 0 & x < 0 \end{cases} \qquad (1)$$

The major problem of LBP is the exponential growth of the number of patterns with respect of the neighborhood size. In order to address this problem, Ojala et al. [10] defined three mapped patterns,which are uniform, rotation invariant and rotation invariant ones, respectively.

The uniform value of an LBP pattern, which is the number of circular spatial transition (bitwise 0/1 or 1/0 changes), can be mathematically computed by

$$U\left(LBP_{R,P}\right) = \sum_{i=0}^{P-1} |s(x_i - x_c) - s(x_{i+1} - x_c)| \qquad (2)$$

When $U\left(LBP_{R,P}\right)$ is less than or equal to 2 i.e U≤2, the pattern is called uniform pattern, denoted as $LBP_{R,P}^{u2}$. Uniform patters have P× (P-1) +3 different output values; these patterns are one of the fundamental patterns within image textures [10].

To achieve rotation invariance, a locally rotation invariance and pattern is defined as follows:

$$LBP_{R,P}^{ri} = \min(ROR\left(LBP_{R,P}, i\right) \quad i = 0,1, \dots P-1) \quad (3)$$

Where$(ROR(x,i))$ denotes bit-wise right shift on the number $x\ i$ times. By introducing the definition of rotation invariance, LBP not only has prominent performance for image rotation, but also has fewer patterns[10].

In order to obtain improved rotation invariance and to further reduce the dimensionality of the LBP histogram feature, building on $LBP_{R,P}^{ri}$, Ojala et al [10] proposed the rotation invariant uniform patterns $LBP_{R,P}^{riu2}$, the collection of those rotation invariance patterns having a U value of at most 2.

$$LBP_{R,P}^{riu2} = \begin{cases} \sum_{i=0}^{p-1} s(x_i - x_c), & if \quad U(LBP_{R,P}) \leq 2 \\ P+1 & otherwise \end{cases} \qquad (4)$$

If P and R are respectively set to 8 and 1 the histogram dimensions of uniform pattern, rotation invariant pattern and rotation invariant uniform pattern are 59, 36 and 10 respectively.

3. Regional Texture descriptors

The regional rank coding is based on the rank of pixel gray scale defined on regional neighborhood. The size and shape of each region depend on the gray level of the treaty pixel.

For each pixel x of the image, we determine the set of pixels forming the tray or plateau containing x noted Pt (x). A plateau is a set of pixels of the same gray level and which are 8 connected (Figure.1). The regional rank coding assigns the same value to all the pixels of the plateau Pt (x), based on gray levels of its neighbors. The set of neighbors of a plateau Pt (x) be the set V (Pt (x)) defined as follows:

$$V(Pt(x)) = \{y \in (Pt(x))^c \ /B8 \ (y) \cap ((Pt(x)) \neq \emptyset\} \qquad (5)$$

Figure.1 represents a partition of an image, we can see two plateau whose gray level equal to 7 (gray color) surrounded by all relevant neighbors (blue color). One of the plateau is composed of five pixels surrounded by sixteen neighbors, while the other plateau is composed of three pixels surrounded by nine neighboring pixels.

12	11	5	4	7	4	4	12
8	4	7	2	2	1	0	11
2	7	7	7	4	2	7	7
11	6	7	4	6	6	7	1
4	6	4	5	7	6	5	8

Figure1.*Representation of plateau and its neighbors*

The gray level of the plateau Pt (x) and all its neighbors are classed in ascending order . If | | V | | is the number of neighbors, the values of possible rank be included in the closed discrete interval [0,. . ., | | V | |].The rank is found according to equation 5.

Considers $V\left(pt(x)\right) = [x_1, x_2, \dots, x_V]$ a set of neighbors of Pt(x) . Let I be the image gray level.

$$rank(x) = \sum_{v=1}^{V} F(x, x_v) \qquad (5)$$

$$F(x, x_v) = \begin{cases} 1 \ if \ I(x) \geq I(x_v) \\ 0 \ if \ I(x) < I(x_v) \end{cases}$$

The found rank will not be used directly to encode the texture because it varies depending on the number of neighbors, then we consider the ratio P0 = rank / | | V | |.

Noting that the plateau Pt(x) and the set of neighbors V(Pt(x)) remains the same even if image is rotated, so ratio P0 is invariant to rotation.

P0 has a continuous value ranging between 0 and 1, hence a quantization is needed; this was done by adding to gether P0 which belonging to the same intervall :[0; 0.25], [0.25;0.5], [0.5;0.75]and [0.75; 1]. P0 aquires an important information , for example, if P0 ∈[0; 0.25], the Pt(x) posseds the minima gray level but if P0 ∈ [0.75. 1] , the corresponded plateau Pt(x) gray level is the maxima amoung its neigbors.

The image gray level has discriminate information. So, to calculate the final coding, a value corresponding to global thresholding of the gray level of the treaty pixel is combined with P0 according to Table 1 .Thus, eight rotation invariant features are extracted.

M represents the average gray level of the whole image I.

I(x) is the gray level of the treaty pixel.

Table1. Regional rank Pattern in function of gray level and ratio P0

	P0 values			
	[0- 0.25[	[0.25 -0.5[	[0.5- 0.75[	[0.75- 1]
I(x)<M	0	1	2	3
I(x)>=M	4	5	6	7

To acquire more information, other scales can be used: features are extracted by extending the search space around each pixel in square neighbourhood of S×S pixel size . The case explained in this section corresponds to S=3.

Figure.2 represents a partition of an image using a square neighborhood of 5×5 pixel size (S=5). We can see plateau whose gray level equal to 7 (graycolor) surrounded by all relevant neighbors (blue color).

The features sizes don't increase with scale and kept constant and equaling to 8.RRC_S corresponds to the features extracted using S× S neighborhood size.

The use of different search space dimension can improve the discriminative power of texture descriptors. So, features extracted from each scale are concatenated in a single feature histogram with n*8 feature dimension where n is number of scales.

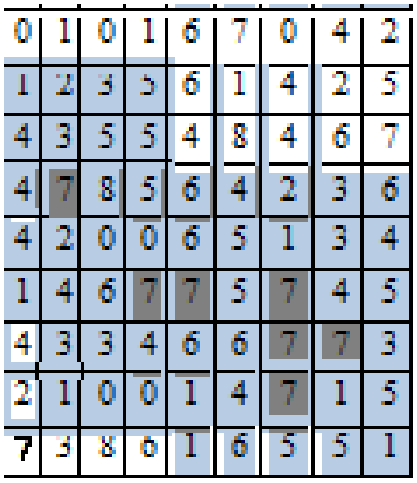

Figure2. *Representation of plateau (green) and its neighbors (blue) using 5× 5 search space .*

4 Experiments and results

The classification performance of the proposed descriptor is compared with state LBP methods on the well known texture databases Outex[11].The Outex database include two test suites: Outex_TC_00010(TC10)andOutex_TC_00012(TC 12).The two suites contain the same 24 classes of textures as shown in Figure.3.Each texture class was collected under three different illuminants("horizon", "inca", and "t184") and nine different rotation angles (0° ,5° ,10° ,15° ,30° ,45° ,60°, 75° ,90°),there are 20non-overlapping 128*128 texture samples for each class under each situation .The experiment setups are as follows: for TC10, samples of illuminant "inca" and angle 0° in each class were used for classifier training and the other eight rotation angles with the same illuminant were used for testing. Hence, there are 480(24*20) models and 3840(24*8*20) validation samples. For TC12, the classifier was trained with the same training samples as TC10, and it was tested with all samples captured under illuminant "t184" or "horizon".Hence, there are 480(24*20) models and 4320(24*20*9) validation samples for each illuminant.

These databases are challenging due to the large number of texture classes, significant rotation and illumination changes. Each texture image is converted into gray scale and normalized to zero mean and unit standard deviation . The nearest-neighborhood classifier χ^2 distance is adopted for the classification task[14].

The proposed method is compared to rotation invariant uniform patterns $LBP_{R,P}^{riu2}$ using different combination. $LBP_{R,P}^{riu2}$feature size are 10, 18 and 26 for R= 1, 2 and 3 respectively.

Table 2 lists the experimental results by different schemes. Under TC12,"t"represents the test setup of illuminant " t184" and "h" represents "horizon".The best results acquired by the proposed methods and LBP are in bold. From the produced results, we can make the following remarks:

First, the RRC_3 classification rate exceeds $LBP_{1,8}^{riu2}$considerably.

Second, histograms concatenated over different scales increase the performance of the methods .So, the best classification rats is obtained by concatenated features histograms extracted from the three scales. We can observe that LBP exceeds slightly the proposed method for TC10 and TC12 "t". But our method exceeds LBP for TC12"h" in different cases . Knowing that the fuzzed LBP feature size 54(10+ 18+26) is about two times the feature size of the fuzzed RRC_S 24(3×8).

Third,RRC_S performance decrease when S increase because the information patterns acquired is more global but less accurate.

Table2.Classification rate (%) on TC10 and TC12 using different Schemes

Methods	Classification Accuracy (%)		
	TC10	TC12 "t"	TC12 "h"
$LBP_{1,8}^{riu2}$	84.81	65.46	63.68
$LBP_{2,16}^{riu2}$	89.40	82.26	75.20
$LBP_{3,24}^{riu2}$	95.07	85.04	80.78
$LBP_{8,1}^{riu2}/LBP_{2,16}^{riu2}$	93.20	84.32	79.35
$LBP_{8,1}^{riu2}/LBP_{3,24}^{riu2}$	**97.65**	**90.76**	**85.25**
$LBP_{2,16}^{riu2}/LBP_{3,24}^{riu2}$	96.40	87.82	82.89
$LBP_{8,1}^{riu2}/LBP_{2,16}^{riu2}$ $/LBP_{3,24}^{riu2}$	97.21	89.21	84.32
RRC_3	92.79	84.42	84.14
RRC_5	86.38	76.97	76.55
RRC_7	79.95	71.06	70.28
RRC_3/ RRC_5	93.91	87.94	87.52
RRC_5/ RRC_7	90.81	81.78	83.43
RRC_3/ RRC_7	94.14	88.77	88.94
RRC_3/ RRC_5 / RRC_7	**94.77**	**88.96**	**89.17**

5. Conclusion

This paper introduced new rotation invariant texture descriptors based on regional rank coding. The features are extracted by combining the regional rank order and the pixel gray level information. Eight rotation invariant features are then extracted. Different neighborhood search space dimension are exploited. Also, the features histogram has the same size in different scales. So, features extracted from each scale are concatenated in a single feature histogram with n*8 feature dimension where n is number of scales.

As demonstrated in the experimental results performed on the Outex database . RRC_3 outperforms $LBP_{1,8}^{riu2}$for TC10 and TC12. RRC_S features produces the best classification rate for TC12 "h" in different cases .

The concactenated histogram features extracted over different scales performs results. The best rate is obtained by using the tree scales exceeding 94% for TC10 and reaching respectively 88.96% and 89.17% for TC 12"t" and TC 12"h".

We think that RRC_3 features has a large area of perspectives to be exploited. Especially to make features more discriminates and eventually robust to noise.

References

[1] Jianguo Zhang, TieniuTan "Brief review of invariant texture analysis methods" pattern recognition35(2002) 735-747.

[2] RM. Haralik, K Shanmugam, I.Dinstein "Texture features for image classification"IEEE Trans Syst Man Cybern 3, (1973) 610–621.

[3] RL. Kashyap, A .Khotanzed "A model-based method for rotation invariant texture classification", IEEE Trans Pattern Anal Mach Intell.8(1986) ,472–481.

.

[4] F.S.Cohen, Z.Fan, M.A.Patel "classification of rotated and scaled textured image using Gaussian markov random field models" IEEE Trans. Pattern Anal. Mach. Intell.13(1991)192-202.

[5] JL .Chen, A. Kundu "Rotation and gray scale transform invariant texture identification using wavelet decomposition and hidden Markov model" IEEE Trans Pattern Anal Mach Intell.16 , (1994) 208–214.

[6] H.Deng and D.A.Clausi, "Gaussian MRF rotation – invariant features for image classification" IEEE Tran. Image Process 26(2004)951-955.

[7] T.Randen and J.Husoy "Filtering for texture classification: A comprative study" IEEE Trans.Pattern Anal.Mach.Intell.21(1999) 291-310.

[8] G.M.Haley and B.S.Manjunath " Rotation–invariant texture classification using a complete space –

frequency model" IEEE Tran. Image Process. 8(1999)255-269.

[9] M. Varma and A. Zisserman "A statistical approach to texture classification from single images" Int. J. Comput. Vision 62, (2005)61–81.

[10] T.Ojala ,M.Pietikainen ,T.Maenpaa, "Multiresolution Gray-Scale and Rotation Invariant Texture Classification with Local Binary Patterns", IEEE Transactions on Pattern Analysis and Machine Intelligence24(2002) 971–987.

[11] T. Ojala, T. Maenpaa, M. Pietikanen, J. Viertola, J. Kyllonen, and S. Huovinen "Outex–New framework for empirical evaluation of texture analysis algorithms", in: Proc. 16th Int. Conf. Pattern Recognit.1(2002) 701–706.

[12] S.Lio, Max W.K.Law and Albert C.S.Chung , "Dominant Local Binary Patterns for Texture Classification", IEEE Transactions on Image Processing18(2009)1107 1117.

[13] Z.Guo,L.Zhang and D.Zhang , "A completed modeling of local binary pattern operator for texture classification", IEEE Tran. Image Process.9(2010)1657-1663.

[14] F.M.Khellah, "Texture Classification Using Dominant Neighborhood Structure", IEEE Tran. Image Process.20(2011)3270-3279.

[15] F. Ouslimani, Z. Ameur , A. Ouslimani, "Texture analysis method using regional rank coding", CNDSP 2014, pp. 353-356, 2014

[16] T.Ojala ,M.Pietikainen ,D.Harwood "A comparative study of texture measures with classification based on features distributions" ,Pattern Recognition29(1996)51-59.

International Journal of Computational and Experimental Science and Engineering (IJCESEN)
Vol. 1-No.2 (2015)pp. 36-40
http://dergipark.ulakbim.gov.tr/ijcesen

***ISSN:*2149-9144**

ResearchArticle

Theoretical and Experimental Investigation of an L-band Chaotic Oscillator

Abdelkader SENOUCİ[1]*, Achour OUSLIMANI[2], Abed-Elhak KASBARI[2], Abdelkrim BOUKABOU[3]

[1]EMP /Bordj El Bahri, Alger-Algérie
[2]ENSEA/ECS-Lab, Cergy-Pontoise, France
[3]Jijel University / Electronics Department, Jijel-Algeria

* CorrespondingAuthor : senouciaek@gmail.com

Presented in "2nd International Conference on Computational and Experimental Science and Engineering (ICCESEN-2015)"

Keywords
ADS
Bifurcation
Chaotic oscillator
Microwave oscillator

Abstract: An L-band microwave buffered chaotic oscillator is designed and realized on a glass teflon hybrid technology. The buffers are optimized in order to match the microwave 50 Ω − 12 GHz oscilloscope without changing significantly the chaotic output characteristic. Dynamical behaviours of the oscillator are theoretically investigated using both numerical studies based on mathematical model and ADS software simulation. First of all, the theoretical study is based on the Matlab simulation, where transistors are modeled by simple mathematical description which is limited only for low frequencies. Nevertheless, it provides a valid approximation to broach a preliminary theoretical investigation. Here, times series, phase portraits, Lyapunov exponents and bifurcation diagrams of the chaotic system are performed. Secondly, in order to account for the increasing frequency, we use the ADS software simulation in which the transistor is described by a high frequency model. Indeed, the impact of microstrip critical lines interconnections and active probes are taken into account in ADS simulations. Spectral and time-domain measurements on the 3.6 GHz spectrum analyzer and 12 GHz oscilloscope are achieved. Experimental characterization gives a fundamental frequency of 2.14 GHz. This microwave chaotic oscillator exhibits attractive spectral characteristics. A good agreement between theoretical and experimental results is obtained.

1. Introduction

Potential applications of chaotic oscillators inspired many researchers to generate broadband chaotic signals [1, 2]. Particular interest is given to the chaotic generators operating in the field of radio frequencies [3, 4, 5]. Besides that, chaotic oscillators have been used for secure communication, data transmission and microwave radar applications [6-9].

Several works using operational amplifiers for generating broadband chaotic signals have been reported in the literature [10, 11]. However, these electronic components operate below the GHz. Moreover, simple circuits, based on the Colpitts oscillator and operable in the macrowave range have been proposed and discussed by several authors [12-17]. Several simulation studies have demonstrated the feasibility of these chaotic generators. However, few practical realizations have been achieved in the radio frequency range. In this work, we present theoretical and experimental investigations of a buffered oscillator for L-band applications.

The oscillator based on microwave transistors with threshold frequency of 9 GHz is realized on a glass teflon hybrid technology. The impact of critical microstrip lines on dynamical behaviour of the oscillator is also investigated.

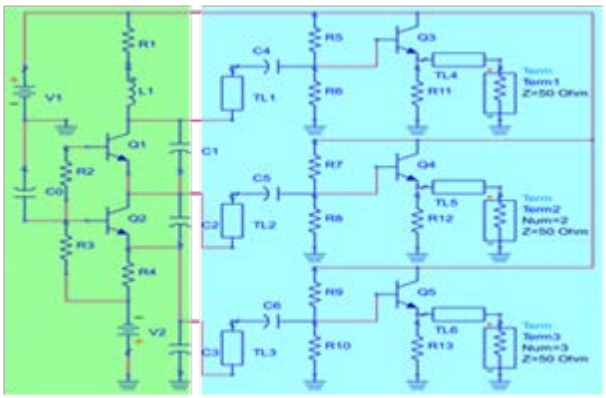

Figure1. *Circuit diagram of the microwave chaotic oscillator.*

2. Theoretical study

The theoretical study is discussed according to the following methodology. First of all, the theoretical study is based on the Matlab simulation, where transistors are modeled by simple mathematical description which is limited only for low frequencies. Nevertheless, it provides a valid approximation to broach a preliminary theoretical investigation. On the other hand, and to take into account the increasing frequency, we use the ADS software simulation in which the transistor is described by complete model taking into account high frequency effects. In this case, the model is more precise and closer to reality.

2.1. Numerical study

The schematic diagram of the chaotic generator is depicted in Fig.1. The resonant circuit consists of resistor R1, the inductor L1, and capacitors C1, C2, and C3. The fundamental frequency of the chaotic generator is given as follows:

$$f_0 = \frac{1}{2\pi\sqrt{LC_{eq}}} \qquad (1)$$

where $\mathrm{Ceq} = \mathrm{C1\,C2\,C3/(C1\,C2 + C1\,C3 + C2\,C3)}$.

Applying the Kirchhoff's laws to the oscillator in the schematic diagram of Fig.1, we obtain the following differential equations:

$$\begin{cases} C_1\dot{V}_{C_1} = I_L - \alpha_1 f(V_{BE_1}) \\ C_2\dot{V}_{C_2} = I_L - I_0 + (1-\alpha_1) f(V_{BE_1}) + (1-\alpha_2) f(V_{BE_2}) \\ C_3\dot{V}_{C_3} = I_L + (1-\alpha_1) f(V_{BE_1}) - \alpha_2 f(V_{BE_2}) \\ L\dot{I}_L = V_0 - V_{C_1} - V_{C_2} - V_{C_3} - RI_L \end{cases} \qquad (2)$$

where $\mathrm{V_{BE_i}(i = 1,2)}$ are the base-emitter voltages of each transistor. These voltages may be expressed in terms of the state vector components as: $\mathrm{V_{BE_1} = V1 - VC2 - VC3}$ and $\mathrm{VBE2 = -VC2}$.

VCi denote the voltages across capacitors Ci, $(\mathrm{i} = 1,2,3)$. f(VBE) is an exponential function expressed by: $\mathrm{I_E = f(V_{BE}) = I_s\left(\exp\left(\frac{V_{BE}}{V_T}\right) - 1\right)}$.

$\mathrm{I_E}$ is the emitter current, and $\mathrm{I_s}$ is the saturation current of the B-E junction. The current source $\mathrm{I_0}$ is used to provide the bias, and $\mathrm{I_L}$ the current flowing through the inductor L. α_i $(i = 1,2)$ are the common-base forward short-circuit current gains.

By neglecting the base currents and setting $x_i = (V_{C_i} - V_{C_i}^0)/V_T$, $(i = 1,2,3)$; $x_4 = \rho(I_L - I_0)/V_T$; $\rho = \sqrt{L/C_2}$; $t = \tau\sqrt{LC_2}$; $\varepsilon = R/\rho$; $\sigma_1 = C_2/C_1$; $\sigma_2 = C_2/C_3$; $\gamma = \rho I_0/V_T$. The dimensionless state-space representation of (2) becomes:

$$\begin{cases} \dot{x}_1 = \sigma_1(x_4 - \gamma\phi(x_2 + x_3)) \\ \dot{x}_2 = x_4 \\ \dot{x}_3 = \sigma_2(x_4 - \gamma\phi(x_2)) \\ \dot{x}_4 = -x_1 - x_2 - x_3 - \varepsilon x_4 \end{cases} \qquad (3)$$

where

$\dot{x}_1 = dx_i/d_\tau$ and $\phi(y) = \exp(-y) - 1$.

$V_T \approx 26\,mV$ at room temperature. $(V_{C_1}^0, V_{C_2}^0, V_{C_3}^0, I_L^0)$ is the equilibrium point obtained by setting the right-hand side of (2) to zero.

In order to define routes to chaos in the microwave chaotic system under study, equations (3) are solved numerically using the standard fourth-order Runge-Kutta algorithm. Two elements can be used to identify the type of transition leading to chaos. The first indicator is the Lyapunov exponent and the second one is the bifurcation diagram.

1) *Lyapunov Exponents*: We take the initial values of the chaotic system (3) as $(x1, x2, x3, x4) = (0.5, 0.5, 1, 1)$ and the parameter values as $\sigma 1 = 4.55$, $\sigma 2 = 1$, $\gamma = 5.95$, $\varepsilon = 1.21$. Then the Lyapunov exponents of the chaotic system (3) are numerically obtained as $\lambda 1 = 0.46; \lambda 2 = 0; \lambda 3 = -0.56;$ $\lambda 4 = -0.69$. Fig.2 depicts the dynamics of the Lyapunov exponents of the chaotic system (3).

2) *Bifurcation analysis*: Each tiny change of any control parameter of the microwave oscillator deserves to be carefully investigated. Our emphasis is on the effect of γ, which have a strong relation with the biasing current I_0. Therefore, to study the sensitivity of the microwave chaotic system, the chosen control parameter was varied in the interval $0.00 < \gamma < 2.00$. Fig.3 illustrates a simulated bifurcation diagram proving the dependence of the dynamical behaviour of the chaotic oscillator on the control parameter. From Fig. 3, we can observe different behaviours of microwave chaotic oscillator including a one-period solution and orbits of increasing period.

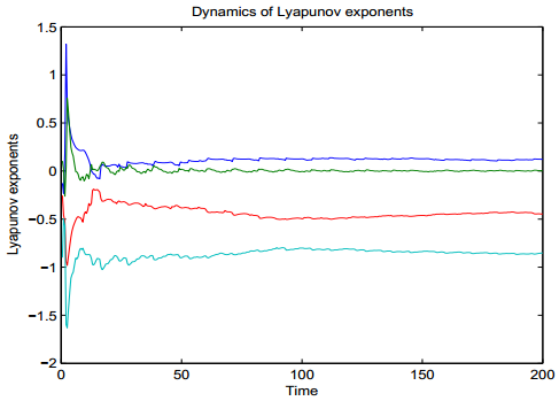

Figure2. *Dynamics of Lyapunov exponents.*

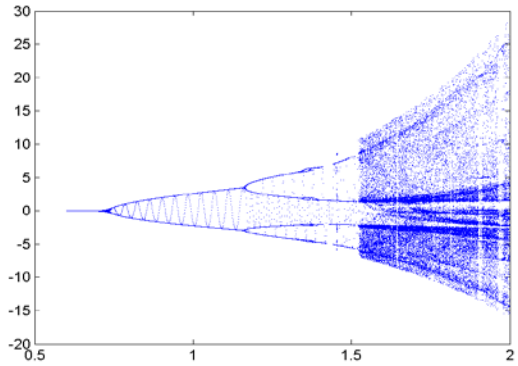

Figure3. *Bifurcation diagram.*

2.1. ADS software simulation

In order to account for the increasing frequency, we use the ADS software simulation in which the transistor is described by a high frequency model. Also, the impact of microstrip critical lines interconnections and active probes are taken into account in ADS simulations. The time series and phase portraits from the ADS simulation are shown in Fig. 6.

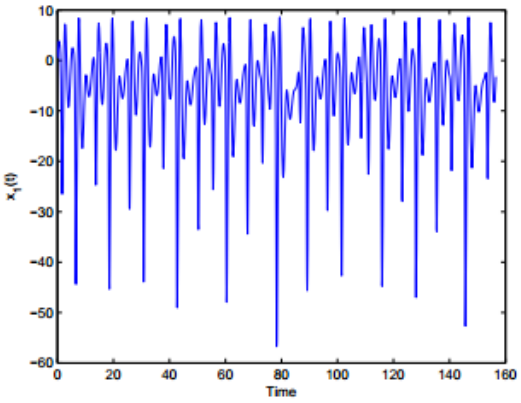

Figure4. *Time evolution of state variables.*

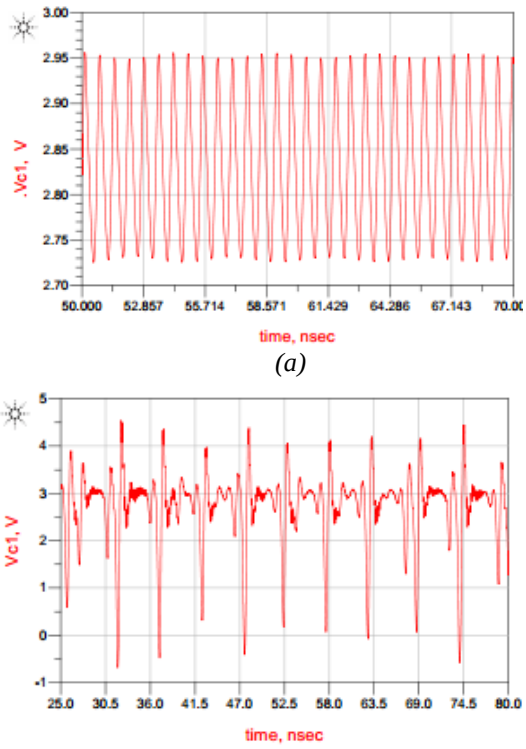

Figure6. *Time evolution of state variables.*

Fig. 5 illustrates the effect of the biasing current I_0 (i.e., control parameter γ) on the dynamics of the circuit oscillator. The variation of I_0 is performed by slowly adjusting the voltage V2. When monitoring the biasing current, we can observe that the electronic circuit presents various types of bifurcation. As depicted in Fig. 5, increasing I_0 results to periodic and chaotic regimes. This is clearly shown by time evolution of the dynamical system under investigation.

3. Experimental validation

Our aim in this part is to verify the theoretical results obtained previously, by carrying out an experimental study. Experimental measurements have been achieved by using a $12\ \text{Ghz} - 40\ \text{GSa/s}$ oscilloscope Agilent DSO 81204B and a 3.6 GHz spectrum analyzer. Therefore, a buffer is used in order to match oscillator outputs with the measuring devices without altering behaviours of the microwave oscillator. Spectral and time-domain measurements on the 3.6 GHz spectrum analyzer and 12 GHz oscilloscope are achieved. Experimental characterization gives a fundamental frequency of 2.14 GHz. This microwave chaotic oscillator exhibits attractive spectral characteristics.

3.1. Design of the experimental circuit

In this section, we expose a hardware implementation of the system (3). Fig.1 illustrates

the electronic circuit that has been designed to realize the system (3). The chaotic microwave oscillator was built using the surface-mount devices and BFG520 bipolar junction transistors. Fig.8 shows the real physical prototype designed and implemented on a bread board.

3.2. Experimental results

By choosing appropriate values for inductance, resistors, capacitors and voltages: L1 = 15nH, R1 = 47Ω, R2 = 22KΩ, R3 = 33KΩ, R4 = 680Ω, R5 = 33KΩ, R6 = 68KΩ, R7 = 33KΩ, R8 = 68KΩ, R9 = 33KΩ, R10 = 68KΩ, R11= 270Ω, R12 = 270Ω, R13 = 270Ω, C0 = 47nF, C1= 2.2pF, C2 = 10pF, C3 = 10pF, C4 = 1nF, C5 = 1nF, C6 = 1nF,V1 = 4V, and by tiny changing the voltage V2 in (0V...10V) range, we realized an experimental electronic circuit for the system (3).

Spectral and time-domain measurements on the 3.6 GHz spectrum analyzer and 12 GHz oscilloscope are achieved. Experimental characterization gives a fundamental frequency of 2.14 GHz. This microwave chaotic oscillator exhibits attractive spectral characteristics. In Fig. 6 are depicted spectral characteristics of one-period, two-period and chaotic signals, respectively. In Fig. 7, we present the time evolution of the microwave outputs. As in ADS simulation, this figure evinces the effect of the biasing current I_0 (i.e., control parameter γ) on the dynamics of the circuit oscillator. By comparing experimental results of Fig.7 and those obtained numerically from Figs. 4, and 5, it can be concluded that a good qualitative agreement between the numerical simulations and the experimental realizations is obtained.

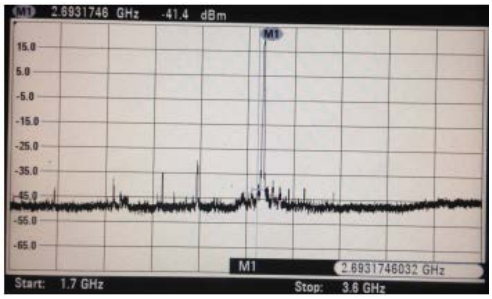

(a) spectrum of the 1-period output

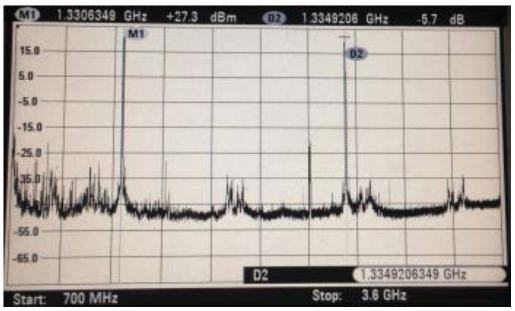

(b) spectrum of the 2-period output

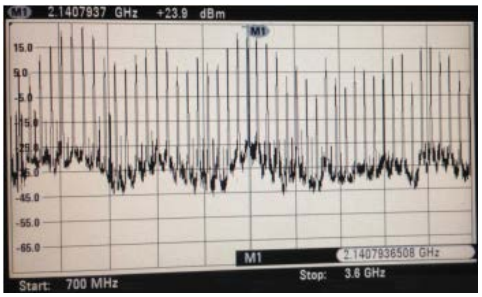

(c) spectrum of the chaotic output

Figure6. *Spectrum of the microwave oscillator outputs.*

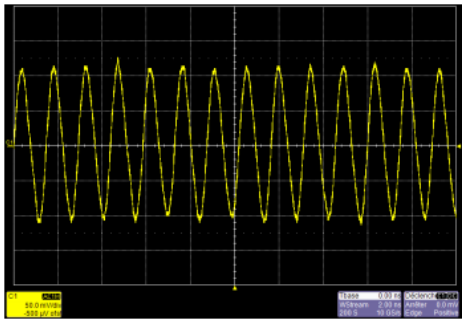

(a) Time evolution of the periodic output

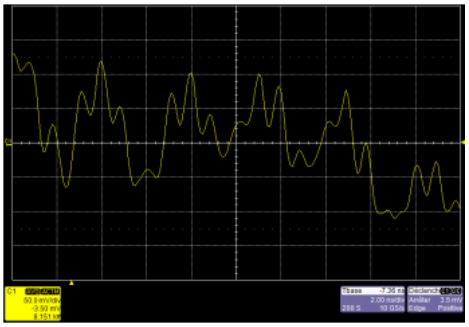

(b) Time evolution of the chaotic output

Figure7. *Time evolution of the microwave oscillator outputs.*

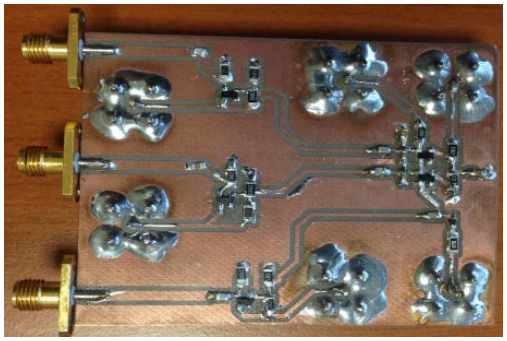

Figure8. *Electronic circuit of the microwave chaotic oscillator.*

4. Conclusion

In summary, we have investigated the bifurcation structures of a microwave chaotic oscillator. The interest devoted to this type of oscillator is mainly due to its multiple potential applications in engineering and in communications. This

microwave chaotic oscillator exhibits attractive spectral characteristics. The electronic structure of the oscillator was first presented and the modeling process was performed to derive a mathematical model describing the behaviour of the oscillator.

The ADS simulations performed with 9 GHz threshold frequency transistors demonstrate that the highest fundamental frequency is 2.14GHz for the proposed microwave chaotic oscillator.

To highlight the effects of bias on the dynamics of the system, I_0 was chosen as the main control parameter. The analysis revealed the extreme sensitivity of the dynamical behaviour of the oscillator to tiny changes in I_0. A real physical prototype was designed and implemented on a bread board.

For designing and realizing this microwave chaotic oscillator, we have considered, during simulations, the increasing frequency, the impact of microstrip critical lines interconnections and active probes.

Acknowledgement

The authors would like to thank the related editors and anonymous reviewers for their useful comments, which have improved this paper.

References

[1] J-G. Wu, L-J. Zhao, Z-M. Wu, D. Lu, X. Tang, Z-Q. Zhong, and G-Q. Xia, Direct generation of broadband chaos by a monolithic integrated semiconductor laser chip, Opt. Express. 21 (2013) 23358-23364

[2] J. Cao, S. Zhou, D. Inman, and Y. Chen, Chaos in the fractionally damped broadband piezoelectric energy generator Nonlinear Dynamics, Springer Netherlands. 80 (2015) 1705-1719

[3] S-M. Han, O. Popov, A. S. Dmitriev, Flexible Chaotic UWB Communication System With Adjustable Channel Bandwidth in CMOS Technology, IEEE Transactions on Microwave Theory and Techniques. 56-10 (2008)2229 - 2236

[4] F. Caudron, A. Ouslimani, R. Vezinet, and A-E. Kasbari, Chaotic behaviour in receiver front-end limiters, Progress In Electromagnetics Research Letters. 23 (2011) 19-28

[5] S. Grishin, E. Zar'kova, and Y.Sharaevskii, Generation of chaotic microwave pulses in broadband self-oscillating ring system with ferro-magnetic film under the action of external pulse-modulated microwave signal Technical, Physics Letters, SP MAIK Nauka/Interperiodica. 37 (2011) 237-240

[6] Z. Shi, S. Qiao, K. Chen, W. Cui, W. Ma, T. Jiang, and L. Ran, Ambiguity functions of direct chaotic radar employing microwave chaotic colpitts oscillator, Progress In Electromagnetics Research. 77 (2007)1–14

[7] A. Senouci, A. Boukabou, K. Busawon, A. Bouridane, and A. Ouslimani, Robust Chaotic Communication Based on Indirect Coupling Synchronization, CSSP. 34 (2015) 393-418.

[8] M. L'Hernault, J.-P. Barbot, and A. Ouslimani, Feasibility of Analog Realization of a Sliding-Mode Observer: Application to Data Transmission, IEEE Transactions on Circuits and Systems I. 55 (2008) 614-624

[9] T. Jiang, S. Qiao, Z. Shi, L. Peng, J. Huangfu, W. Cui, W. Ma, and L. Ran, Simulation and experimental evaluation of the radar signal performance of chaotic signals generated from a microwave colpitts oscillator, Progress In Electromagnetics Research. 90 (2009)15–30

[10] A. S. Elwakil, M. P. Kennedy, Inductorless hyperchaos generator, Microelectronics Journal. 30 (1999)739–743

[11] F. R. Tahir, S. Jafari, V-T. Pham, C. Volos, and X. Wang, A Novel No-Equilibrium Chaotic System with Multiwing Butterfly Attractors, International Journal of Bifurcation and Chaos. 25-4 (2015)

[12] M. P. Kennedy, Chaos in Colpitts oscillator, IEEE Trans. Circuits Syst. I. 41 (1994)771–774

[13] S. Bumeliene, A. Tamasevicius, G. Mykolaitis, A. Baziliauskas, and E. Lindberg, Numerical investigation and experimental demonstration of chaos from two-stage Colpitts oscillator in the ultrahigh frequency range, Nonlinear Dyn. 44 (2006)167–172

[14] J. X. Li, Y. C. Wang, and F. M. Chang, Experimental demonstration of 1.5 GHz chaos generation using an improved Colpitts oscillator, Nonlinear Dynamics. (2013)

[15] J. Kengne, J. C. Chedjou, G. Kenne, and K. Kyamakya, Dynamical properties and chaos synchronization of improved Colpitts oscillators, Commun Nonlinear Sci. Numer. Simul. 17 (2012)2914–23

[16] A. Buscarnio, L. Fortuna, M. Frasca, and G. Sciuto, Coupled inductor based Colpitts oscillator, Int J Bifurcation Chaos. 21 (2011)569–74

[17] G. M. Maggio, O. D. Feo, and M.P. Kennedy, Nonlinear analysis of the Colpitts oscillator and applications to design, IEEE Trans Circuits Syst – I. 46 (1999) 1118–29.

International Journal of Computational and Experimental Science and Engineering (IJCESEN)
Vol. 1-No.2 (2015) pp. 41-45
http://dergipark.ulakbim.gov.tr/ijcesen

ISSN: **2149-9144**

Research Article

Three Dimensional Simulation of Heat and Mass Transfer During Facing Brick Drying[#]

Ramzi RZIG[1]*, Nidhal BEN KHEDHER[2], Sassi BEN NASRALLAH[3]

[1]National School of Engineers of Monastir, Energetic Department, 5019, Monastir-Tunisia
[2]College of Engineering, Mechanical Engineering Department, Haïl University, 2440, Haïl City-Saudi Arabia
[3]National School of Engineers of Monastir, Energetic Department, 5019, Monastir-Tunisia

* Corresponding Author : rzigramzi10@gmail.com

[#] Presented in "2nd International Conference on Computational and Experimental Science and Engineering (ICCESEN-2015)"

Keywords
3-D drying
Facing brick
CVFEM
Gmsh

Abstract: This work is devoted to presenting a 3-D drying of facing brick from two perspectives: theory and industrial practice. A Three-dimensional unstructured Control Volume Finite Element Method (CVFEM) is developed in order to simulate unsteady coupled heat and mass transfer phenomena that arise during convective drying of unsaturated porous media. In order to simulate 3-D complex geometries, as application here the drying of facing brick, we used the free mesh generator Gmsh. Several simulation results are presented that depict the new possibilities offered by such a tool. In particular, the simulation of a whole facing brick at the industrial scale.
This simulation proves that only three spatial dimensions are able to explain the heat and mass transfer during drying process. Indeed, thanks to this 3-D tool and unlike 2-D model we can observe for the first time unexpected thermal field, liquid saturation and pressure distributions for whole facing brick at the industrial scale and hence evaluating the correct drying rate under the real conditions.

1. Introduction

Drying which is a classical problem of transport in porous media is one of the most energy intensive industrial processes with applications in a wide variety of industries but its scientific understanding requires considerable efforts. Consequently, considerable researches have been conducted to numerically simulate the drying process. Drying is a process involves a coupled heat and mass transfer in a multi-phase flow in porous media. Based on the theory proposed by drying Luikov [1] and later by Whitaker [2], several mathematical models for drying porous materials have been developed. The first digital studies began on simple geometry and easy to discretize in regular and Cartesian grid. In this context some methods have been developed. In addition, the finite difference method has been widely used in the numerical simulation of mass and heat transfer in porous media. Moreover, this method may causes numerical dispersion and grid orientation problems [3]. It also gives rise to difficulties in the treatment of complicated geometry and boundary conditions. To overcome these deficiencies, the intrinsic grid flexibility of the finite element method has been utilized [4], but this method does not conserve mass locally. Recently, the Control Volume Finite Element Method (CVFEM) has been developed to enforce such a conservation property [5].
Thus, this work presents a contribution to the establishment by MVCEF of a digital three-dimensional simulation of heat and mass transfer during drying of unsaturated porous media with complex geometries.

2. Mathematical model

The proposed problem, which is described by Figure 1, is an industrial problem treating the drying of whole facing brick.

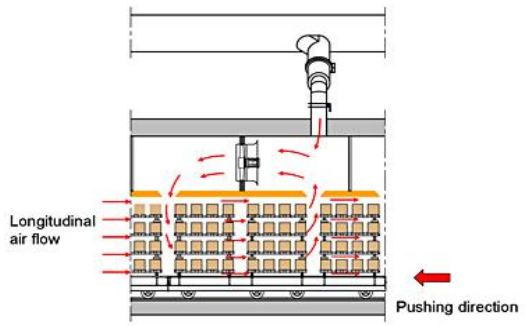

Figure 1. *Industrial dryer of facing bricks.*

The system considered in this work is a facing brick (Figure 2) which is composed of:

- An inert and rigid solid phase (brick matrix).

- A liquid phase (pure water).

- A gaseous phase which contains both air and water vapor.

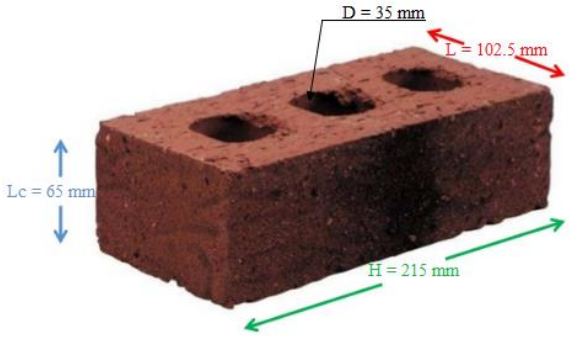

Figure 2. *Facing brick dimensions.*

2.1. Governing equations

Inspiring by Whitaker theory [2], a mathematical model governing heat and mass transfer is established for the unsaturated porous media.
In order to obtain a closed set of governing macroscopic equations, the following assumptions are made:

- The porous layer is homogenous and isotropic.
- The solid, liquid and gas phases are in local thermodynamic equilibrium.
- The compression-work and viscous dissipation are negligible.
- The gas-phase is ideal in the thermodynamic sense.
- The dispersion and tortuosity terms are interpreted as diffusion term.
- The radiative heat transfer is negligible.

Considering these assumptions, macroscopic equations governing heat and mass transfer in the porous medium are:

- Mass conservation equations:

For liquid phase:

$$\frac{\partial \varepsilon_l}{\partial t} + \nabla(\overline{V_l}) = -\frac{\dot{m}_v}{\overline{\rho}_l} \quad (1)$$

For Vapor phase:

$$\frac{d\overline{\rho_v}}{dt} + \nabla\left(\overline{\rho_v}^g \overline{V_v}\right) = \dot{m}_v \quad (2)$$

$$\overline{\rho_v}^g \overline{V}v = \overline{\rho_v}^g \overline{V}g - \overline{\rho_g}^g D_{eff} \nabla\left(\frac{\overline{\rho_v}}{\overline{\rho_g}^g}\right) \quad (3)$$

- Energy conservation equation:

$$\frac{\partial}{\partial t}\left(\overline{\rho C_p}\,\overline{T}\right) + div\left[\left(\overline{\rho_l}^l C_{pl}\,\overline{v_l} + \sum_{k=a,v} \overline{\rho_k}^g C_{pk}\,\overline{v_k}\right)\overline{T}\right] = \nabla\left(\lambda_{eff}.\nabla\overline{T}\right) - \Delta H_{vap}.\dot{m}_v \quad (4)$$

2.2. Boundary and initial conditions

Initially, the temperature, the gas pressure and liquid saturation are uniform in the brick, as shown in Figure 3.
Thermal energy brought by air convection is necessary for water evaporation and to the heat conduction in porous medium. This energy is function of temperature and heat transfer coefficient.

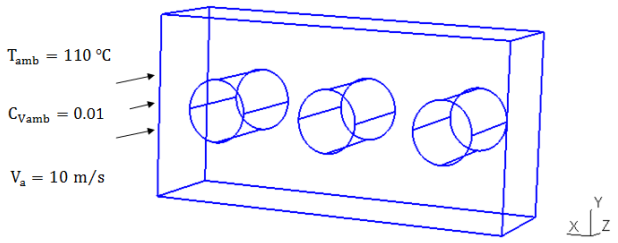

Figure 3. *Operating conditions of drying process.*

3. Solution method

The equations set, with initial and boundary conditions has been solved numerically using the Control Volume Finite Element Method (CVFEM).
For the mesh generation (Figure 4), we use the free mesh generator "**Gmsh**".

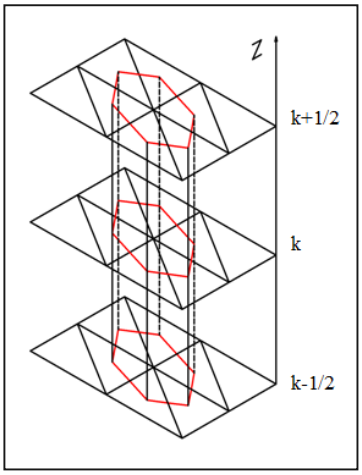

Figure 4. *Control volume and sub-volume.*

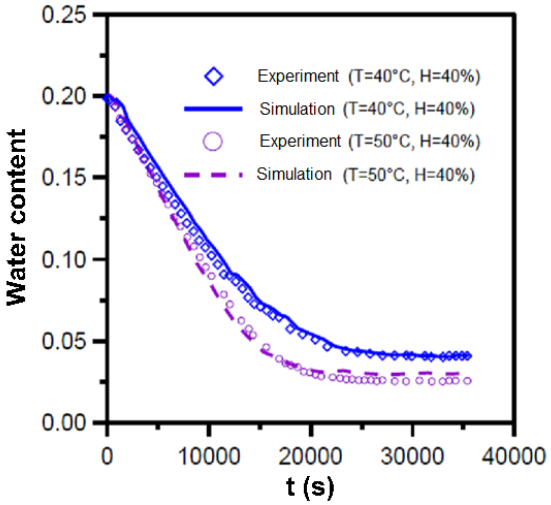

Figure 5. *Comparison of numerical and experimental of average water content.*

4. Experimental validation

The coupled heat and mass transfer model is validated by means of a convective drying experiment developed by Saber CHEMKHI [6].
The experiment was conducted on a rectangular plate size (15x12x1.5 cm^3).
The operating conditions used are presented in Table 1.

Table 1. *Operating conditions for the validation*

$T_{amb}\ (°C)$	40	50
$T_{ini}\ (°C)$	25	
$Initial\ water\ content\ (kg/kg\ b.s)$	0.1995	
C_{Vamb}	0.01	
$P_{amb}\ (atm)$	1	
$Relative\ humidity\ (\%)$	40	
$Air\ velocity\ (m/s)$	2	

Referring to Figure 5, which shows the time evolution of the water content, there is overall good agreement between the numerical results and the experimental data.

5. Results and discussions

The operating conditions are takers the same of a typical industrial drying process which are listed in Table 2.

Table 2. *Operating conditions.*

T_{amb} (°C)	T_{ini} (°C)	S_{ini} (%)	C_{Vamb}	P_{amb} (atm)	P_{ini} (atm)
110	20	50	0.01	1	1

From the time evolution of temperature, liquid saturation and gaseous pressure for five nodes aligned along the z axis which are depicted in Figure 6, we can clearly observe the three conventional drying phases:

- The transient heating phase
- The constant drying rate phase
- The decreasing drying rate phase:
  - First decreasing drying rate period
  - Second decreasing drying rate period

In order to better observe the mechanisms of drying, we have shown in Figure 7 the spatiotemporal evolutions of temperature, liquid saturation and gaseous pressure during the drying of facing brick.

Figure 7 represents the distribution of the temperature, the liquid saturation and the gaseous pressure of the drying of facing brick at 5 h of drying.

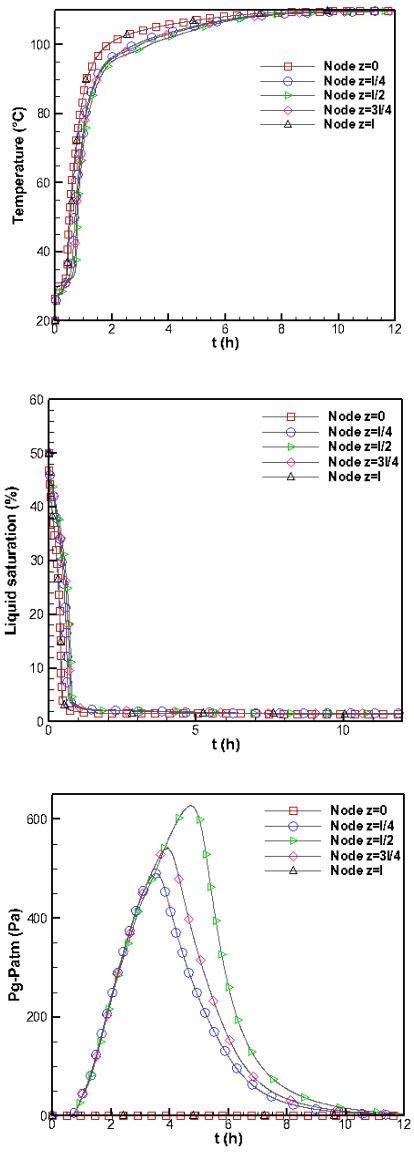

Figure 6. *Evolution of temperature, liquid saturation and pressure for five nodes aligned along the z axis.*

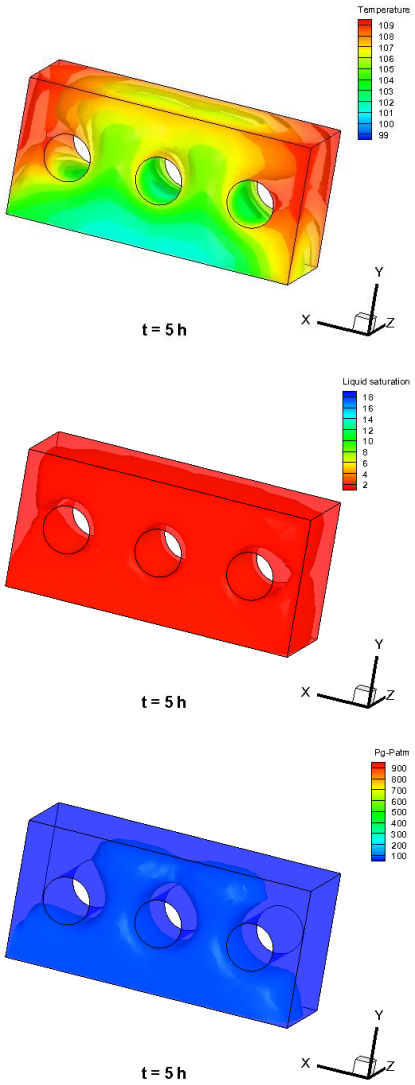

Figure 7. *Distribution of the temperature, the liquid saturation and the gaseous pressure inside facing brick.*

The presence of three orthogonal exchanging faces forces the liquid saturation to be very low at the corners and given the fact of the gravity, it is clear that only the core of facing brick retains a high value of liquid saturation. Moreover, the temperature and pressure fields allow more subtle phenomena to be observed. The temperature gradient is required to supply the energy necessary for the evaporation which occurs rapidly and intensively near the exchanging faces. Also the temperature varies significantly in space only in the region of vapor migration (gaseous Darcy's flow and vapor diffusion). The pressure gradient that exists in this region results from a cross diffusion effect of vapor and air, and in the domain of free water, almost no pressure gradient exists.

6. Conclusions

For the first time, a 3-D drying model that is able to deal with a comprehensive set of macroscopic equations for three-dimensional drying of a whole facing brick at the industrial scale has been established.

From the presented numerical results that highlight the phenomena accompanying the drying of unsaturated porous media (facing brick), we can conclude that:

- The model successfully simulates the appearance and the evolution of the different phases of convective drying.
- The model allows simulating problems of heat and mass transfer for three-dimensional complex geometries.

- The physical analysis presented in this work highlights the ability of this code to be closer to reality than every before.

In the end, the new 3-D version of heat and mass transfer during drying of facing brick appears to be a very promising tool for improving the understanding of the drying process and therefore shows the limitations of the two-dimensional numerical studies to solve this kind of problems.

Nomenclature

C_a specific heat of the air $[kJ/kgK]$
C_p specific heat at constant pressure $[kJ/kgK]$
C_v specific heat of the vapor $[kJ/kgK]$
C_w specific heat of the water $[kJ/kgK]$
$D_{A,B}$ diffusion coefficient [m^2/s]
D holes diameter [m]
g gravitational acceleration [m/s^2]
h_m convective mass transfer coefficient[$W/m^2°C$]
h_t convective heat transfer coefficient[$W/m^2°C$]
K intrinsic permeability [m^2]
L_c characteristic length of brick [m]
M_a molar mass of air [kg/mol]
M_v molar mass of vapour [kg/mol]
$\dot{m}$ evaporation rate [kg/s]
n_i outward normal vector
P pressure [Pa]
Pc capillary pressure [Pa]
P_{Vs} partial pressure of saturated vapour [Pa]
R gas constant $[J/Kmol]$
r characteristic magnitude that represents the average radius of curvature of the menisci if the retention forces of the liquid are of capillary origin
S liquid saturation [%]
T temperature [K]
t time [s]
w_a air velocity $[m/s]$

Greek symbols

ε porosity
ε_l volume fraction of liquid phase
μ dynamic viscosity [kg/ms]
ϑ cinematic viscosity $[m^2/s]$
ρ density [kg/m^3]
λ conductive transfer coefficient $[W/m°C]$
σ surface tension $[N/m]$
ΔH_{vap} vaporisation latent heat [J / Kg]

Subscripts

0 initial condition
A air
eff effective
g gas
l liquid
v vapour

Dimensionless groups

R_e Reynolds number
P_r Prandtl number
S_c Schmidt number

References

[1] A.V.Luikov "Systems of differential equations of heat and mass transfer in capillary porous bodies (review)" Int. J. Heat Mass Transfer. 18 (1975)1–14.

[2] S.Whitaker "Simulation heat, mass and momentum transfer in porous media a theory of drying" Advances in Heat Transfer. Vol. 13, pp. 119-203. Academic Press. New York, 1977.

[3] Z.Chen, R.E.Ewing, Z.-C.Shi (eds.) "Numerical treatment of multiphase flows in porous media" Lecture Notes in Physics. Vol. 552, Heidelberg: Springer 2000.

[4] R.E.Ewing (ed.) "The mathematics of reservoir simulation" Philadelphia: SIAM 1983.

[5] L.S.Fung, A.D.Hiebert, L.Nghiem "Reservoir simulation with a control volume finite element method" SPE 21224. 11th SPE Symp. on Reservoir Simulation. Anaheim, 17-20 February, 1991.

[6] S.Chemkhi "thesis Drying of an unsaturated deformable middle: modeling of hygro-mechanical coupling" doctoral dissertation, Bordeaux 1 University, 2008.